

1 **Transport-driven aerosol differences above and below the canopy of**  
2 **a mixed deciduous forest**

3 Alexander A.T. Bui<sup>1</sup>, Henry W. Wallace<sup>1, a</sup>, Sarah Kavassalis<sup>2</sup>, Hariprasad D. Alwe<sup>3</sup>, James H. Flynn<sup>4</sup>,  
4 Matt H. Erickson<sup>4, b</sup>, Sergio Alvarez<sup>4</sup>, Dylan B. Millet<sup>3</sup>, Allison L. Steiner<sup>5</sup>, Robert J. Griffin<sup>1, 6</sup>

5 <sup>1</sup>Department of Civil and Environmental Engineering, Rice University, Houston, TX, 77005, USA

6 <sup>2</sup>Department of Chemistry, University of Toronto, Toronto, ON, M5S 3H6, Canada

7 <sup>3</sup>Department of Soil, Water, and Climate, University of Minnesota, St. Paul, MN 55108, USA

8 <sup>4</sup>Department of Earth and Atmospheric Sciences, University of Houston, Houston, TX, 77204, USA

9 <sup>5</sup>Department of Climate and Space Sciences and Engineering, University of Michigan, Ann Arbor, MI, 48109, USA

10 <sup>6</sup>Department of Chemical and Biomolecular Engineering, Rice University, Houston, TX, 77005, USA

11 <sup>a</sup>now at: Washington State Department of Ecology, Lacey, WA, 98503, USA

12 <sup>b</sup>now at: TerraGraphics Environmental Engineering, Pasco, WA, 99301, USA

13 *Correspondence to:* Robert J. Griffin (rob.griffin@rice.edu)

14 **Abstract.** Exchanges of energy and mass between the surrounding air and plant surfaces occur below, within, and above a  
15 forest's vegetative canopy. The canopy also can lead to vertical gradients in light, trace gases, oxidant availability, turbulent  
16 mixing, and properties and concentrations of organic aerosols (OA). In this study, a high-resolution time-of-flight aerosol  
17 mass spectrometer is used to measure non-refractory submicron aerosol composition and concentration above (30m) and  
18 below (6m) a forest canopy in a mixed deciduous forest at the Program for Research on Oxidants: Photochemistry,  
19 Emissions, and Transport tower in northern Michigan during the summer of 2016. Three OA factors are resolved using  
20 positive matrix factorization: more-oxidized oxygenated organic aerosol (MO-OOA), isoprene-epoxydiol-derived organic  
21 aerosol (IEPOX-OA), and 91Fac (a factor characterized with a distinct fragment ion at  $m/z$  91) from both the above- and  
22 below-canopy inlets. MO-OOA was most strongly associated with long-range transport from more polluted regions to the  
23 south, while IEPOX-OA and 91Fac were associated with shorter-range transport and local oxidation chemistry. Overall  
24 vertical similarity in aerosol composition, degrees of oxidation, and diurnal profiles between the two inlets was observed  
25 throughout the campaign, which implies that rapid in-canopy transport of aerosols is efficient enough to cause relatively  
26 consistent vertical distributions of aerosols at this scale. However, four distinct vertical gradient episodes are identified for  
27 OA, with vertical concentration differences (above-canopy minus below-canopy concentrations) in total OA of up to 0.8  
28  $\mu\text{g}/\text{m}^3$ , a value that is 42% of the campaign average OA concentration of  $1.9 \mu\text{g}/\text{m}^3$ . The magnitude of these differences  
29 correlated with concurrent vertical differences in either sulfate aerosol or ozone. These differences are likely driven by a  
30 combination of long-range transport mechanisms, canopy-scale mixing and local chemistry. These results emphasize the  
31 importance of including vertical and horizontal transport mechanisms when interpreting trace gas and aerosol data in  
32 forested environments.

33

**Deleted:**

**Deleted:**

36 **1 Introduction**

37       Aerosols play a key role in the energy balance of the Earth's climate system by scattering and absorbing incoming solar  
38 radiation and by impacting cloud lifetime and reflectivity (IPCC, 2007). These climatic effects depend strongly on the  
39 chemical speciation of the aerosol particles. Approximately 20-90% of submicron aerosol mass worldwide on average has  
40 been predicted to be organic material (Kanakidou et al., 2005), and this is supported by field studies in a variety of urban,  
41 urban downwind, and rural locations across the Northern Hemisphere (Jimenez et al., 2009; Zhang et al., 2007). The bulk of  
42 this organic material is thought to be secondary organic aerosol (SOA), which is formed in the atmosphere by the reaction of  
43 volatile organic compounds (VOCs) with oxidants such as hydroxyl radical (OH), ozone ( $O_3$ ), nitrate radical, and chlorine  
44 atom, with the resulting products then partitioning to the particle phase.

45       Precursor VOCs that contribute to SOA formation are emitted from both anthropogenic and biogenic sources. Biogenic  
46 VOCs (BVOCs) primarily are emitted into the atmosphere from terrestrial vegetation, and on a global scale, emissions of  
47 BVOCs exceed those of anthropogenic VOCs (Fehsenfeld et al., 1992; Guenther et al., 2000, 1995). Major SOA precursor  
48 BVOCs include isoprene ( $C_5H_8$ ) and terpenes. To date, more than 5000 terpene compounds have been identified, including  
49 monoterpenes ( $C_{10}$ ), sesquiterpenes ( $C_{15}$ ), and diterpenes ( $C_{20}$ ) (Geron et al., 2000). However, factors such as the addition  
50 of functional groups (aldehydes, alcohols, carboxylic acids, alkyl nitrate, etc.) and the wide variety of possible reaction  
51 pathways rapidly increase the number of relevant atmospheric VOCs beyond what is initially emitted (Goldstein and  
52 Galbally, 2007).

53       If other loss processes, including deposition, were not considered, the final atmospheric fate of the carbon associated  
54 with BVOCs would be oxidation to carbon dioxide. However, partitioning of oxidation products to the aerosol phase as  
55 SOA interrupts this oxidation sequence. Partitioning of VOC oxidation products between the gas and aerosol phases  
56 depends on multiple factors such as the phase and concentration of pre-existing primary OA (POA) or SOA, particulate-  
57 phase SOA reactions, and the presence of aerosol liquid water (ALW) (Seinfeld and Pandis, 2006). As a result of the large  
58 number of precursor VOCs, the highly non-linear oxidation chemistry, and the presence of multiple aerosol phases in the  
59 atmosphere, SOA formation is complex and relatively poorly understood (Goldstein and Galbally, 2007).

60       The physical environment strongly impacts these chemical SOA formation processes. For example, in forested areas in  
61 which BVOC emissions are prevalent, the exchanges of energy and mass between the forest and the atmosphere are  
62 influenced by the forest's vegetation canopy. Absorption of light by a canopy can diminish the amount of radiation that is  
63 received below the canopy, influencing photolysis rates of photolabile species (Balocchi et al., 1995; Brown et al., 2005;  
64 Fuentes et al., 2007; Makar et al., 2017; Schulze et al., 2017) and oxidant availability (Fuentes et al., 2007). Loss of BVOC  
65 oxidation products to deposition within the canopy also has been found to be an important factor in determining the  
66 oxidative capacity of a forested environment (Pugh et al., 2009).

67       Vertical transport, also influenced by the canopy, likewise impacts the concentrations of BVOC and SOA in forested  
68 environments. Roughness elements created by the leaves, branches, and stems in a dense vegetative canopy combined with  
69 above-canopy wind shear leads to coherent structures (Finnigan, 2000). These turbulent flow structures contribute to the  
70 fluxes of heat, energy, and matter in forest canopies (Thomas and Foken, 2007). The physical motion of coherent structures  
71 occurs via two main mechanisms: upward "bursts," in which air is ejected upward from the canopy into the atmosphere, and  
72 downward "sweeps," in which air is directed downward from the atmosphere into the canopy. Vertically resolved sonic  
73 anemometer measurements, which provide temperature and three-dimensional wind velocity components at each vertical  
74 measurement location, can be used to derive in-canopy mixing metrics.

75       The relative magnitudes of timescales for turbulent transport and chemical processing govern how trace compounds are  
76 distributed within the canopy (Balocchi et al., 1995; Fuentes et al., 2007; Steiner et al., 2011). A modeling study by Gao et  
77 al. (1993) found that in-canopy chemical processing of isoprene occurs on a much longer timescale than turbulent transport,  
78 making in-canopy reactions less important compared to the turbulent transport and emission of isoprene in determining its

79 in-canopy concentrations. On the other hand, for compounds with an estimated chemical loss timescale that is roughly  
80 equivalent to the timescales of turbulent transport (e.g., O<sub>3</sub>-initiated oxidation of the sesquiterpene  $\beta$ -caryophyllene), rapid  
81 in-canopy chemical loss could dominate (Stroud et al., 2005). Furthermore, partitioning to the aerosol-phase was inferred as  
82 a potential reason for observations of decreased mixing ratios of oxidation products of very reactive BVOCs in a ponderosa  
83 pine forest canopy (Holzinger et al., 2005).

84 Several studies have attempted to model vertical profiles of trace gases and aerosols in a forest canopy considering both  
85 chemistry and turbulent transport. Bryan et al. (2012) found that forest canopy-atmosphere interactions were highly  
86 sensitive to turbulent mixing parameterizations during a field campaign in northern Michigan. Differences in highly reactive  
87 BVOCs and BVOC oxidation products have been estimated above and below the canopy in modeling and measurement  
88 efforts (Alwe et al., 2019; Ashworth et al., 2015; Holzinger et al., 2005; Schulze et al., 2017; Stroud et al., 2005; Wolfe and  
89 Thornton, 2011). Schulze et al. (2017) found that rapid through-canopy transport (minimum in-canopy residence time of 10  
90 min) leads to relatively consistent simulated above- and below-canopy SOA composition and concentration.

91 Because in-canopy mixing plays a role in the vertical distribution of trace gases and aerosols in a forest canopy, vertical  
92 differences in OA components and other inorganic aerosol species such as sulfate (SO<sub>4</sub>) could be caused by the degree of  
93 mixing between the above- and below-canopy environments. During the PROPHET-CABINEX 2009 campaign, the degree  
94 of atmosphere-canopy coupling between the above-canopy atmosphere and the forest was analyzed by Steiner et al. (2011).  
95 In this study, the degree of coupling was calculated using the ratio of the kinematic heat flux above the canopy to the  
96 kinematic heat flux in the upper canopy. Opposing kinematic heat flux directions (negative ratios) imply that the below-  
97 canopy environment is uncoupled from the atmosphere. In 2009, coupling conditions ranged between strong coupling  
98 (greater than zero but less than the threshold value defined by the slope of a regression between the two heat fluxes), weak  
99 coupling (greater than the defined threshold value), and uncoupled (negative). Uncoupled conditions occurred most  
100 commonly in the early morning hours between 4AM and 8AM local time. This set of hours represents approximately 30%  
101 of every day over the whole 2009 study period. This suggests that early morning hours may contribute to more instances of  
102 uncoupled canopy-atmosphere conditions but that coupling between the forest canopy and the atmosphere occurs a majority  
103 of the time (Steiner et al., 2011).

104 Past field studies, such as those above a tropical forest in Brazil and a temperate forest in California, found that in-  
105 canopy SOA formation, deposition, and thermal gradient effects on gas-particle partitioning all influence net OA fluxes  
106 (Farmer et al., 2013). In the same study, the authors found that oxygenated OA tended to deposit in the canopy, whereas the  
107 forest canopy released less oxygenated OA. The source of OA fluxes between forests and the atmosphere has been  
108 associated with vertical turbulent transport between the forest atmosphere and the surface layer directly above the canopy;  
109 however, there have been few studies that have provided high temporal resolution measurements of both OA composition  
110 throughout a forest canopy and canopy mixing strength. In a mixed forest in Ontario, Canada, Gordon et al. (2011) found  
111 that the frequent occurrence of net upward aerosol flux was associated with decoupled canopy conditions where entrainment  
112 of particle-free air from above the canopy created a positive flux above the forest. On the other hand, Whitehead et al.  
113 (2010) found that the particle number concentration and submicron particle composition in the trunk space (i.e., below-  
114 canopy) and above-canopy environments showed minimal variation with height during daytime due to stronger turbulence  
115 and mixing conditions. In light of these limited studies, there is a need for additional measurements and data to inform the  
116 exchange of aerosols between the forest and the atmosphere.

117 Recent work from the Program for Research on Oxidants and PHotochemistry, Emissions and Transport (PROPHET)  
118 during the Atmospheric Measurements of Oxidants in Summer (AMOS) campaign in 2016 has indicated that flux of  
119 isoprene and monoterpenes at the canopy-atmosphere boundary represents over half of the net carbon flux, while oxygenated  
120 VOCs (OVOCs) constitute a majority of the species with detectable VOC fluxes (192 of the 236 species with identified  
121 molecular formulas). The authors report that the observed and modelled net carbon flux during the campaign was upward  
122 (canopy emission) during the campaign in 2016 (Millet et al., 2018). Vertical gradients of BVOCs in this mixed forest  
123 environment vary greatly depending on canopy vegetation height, primary emission versus secondary production, and  
124 diurnal variability (Alwe et al., 2019). Correlation analysis of VOC vertical gradients suggests that formic acid (HCOOH)

**Formatted:** Font: (Default) Times New Roman

**Deleted:** In 2009, coupling conditions ranged between strong coupling, weak coupling, and uncoupled. Uncoupled conditions

127 originates from a secondary photochemical production. During the same campaign, distinct sample-to-sample variability in  
128 the molecular-level aerosol composition (73 +/- 8%) was observed despite less variability in elemental composition of the  
129 bulk OA, indicating the chemical complexity of functionalized OA at the site (Ditto et al., 2018).

130 Here, measurements using an Aerodyne high-resolution time-of-flight aerosol mass spectrometer (HR-ToF-AMS) are  
131 used to characterize ambient aerosol above and below the canopy in a mixed, deciduous forest during the PROPHET-AMOS  
132 campaign in 2016, with the aim of evaluating quantitatively potential chemical and physical phenomena leading to observed  
133 differences between particulate matter above and below the forest canopy. These measurements provide data for validation  
134 of forest canopy-atmosphere exchange models and allow an assessment of turbulent transport in the forest canopy and the  
135 resulting impacts on above- and below-canopy SOA composition and concentration. These data also could assist in the  
136 determination of whether or not SOA is forming within the forest canopy.

Formatted: Font: (Default) Times New Roman

## 137 2 Methods

### 138 2.1 Site description

139 Measurements were made during the PROPHET-AMOS 2016 campaign from 1 July – 31 July 2016. The PROPHET  
140 site (45.55° N, 84.78° W) is situated in a temperate, mixed deciduous forest in the northern portion of Michigan's Lower  
141 Peninsula at the University of Michigan Biological Station (UMBS). The surrounding forest consists of aspens (60.9%),  
142 northern hardwoods (16.6%; maple, beech, birch, ash, and hemlocks), upland conifers (13.3%; white and red pines), non-  
143 forest cover types (7.6%; bracken ferns/grass/developed/road), and northern red oak (1.6%) (Cooper et al., 2001; Bergen and  
144 Dronova, 2007). The forests in this region are currently undergoing succession, where the dominant aspens have matured  
145 and are now being replaced by northern hardwoods and pines (Bergen and Dronova, 2007). It is expected that this new  
146 forest composition will shift BVOC emissions from an isoprene-dominated environment to one that is more influenced by  
147 monoterpenes (Toma and Bertman, 2012). The height of the forest canopy varies, but the mean canopy height is  
148 approximately 22.5 meters (VanReken et al., 2015). The site's physical layout and site meteorology have been described  
149 elsewhere (Carroll et al., 2001; Cooper et al., 2001). The PROPHET site features a 31-m scaffolding tower, allowing  
150 measurements to be made at variable heights within and above the vegetation canopy.

151 Due to the sparse surrounding population, the PROPHET site at UMBS has minimal local anthropogenic influences.  
152 The closest major urban centers include Detroit, Michigan (350 km to the southeast, population: 672,795), Milwaukee,  
153 Wisconsin (350 km to the southwest, population: 595,047), and Chicago, Illinois (450 km to the southwest, population:  
154 2,704,958) (Carroll et al., 2001). The closest nearby towns include Pellston, Michigan (5 km to the west, population: 828),  
155 Petoskey, Michigan (30 km to the southwest, population: 5,749), and Cheboygan, Michigan (30 km to the northeast,  
156 population: 4,726). Population totals are based on 2016 population estimates for cities and towns in the United States (US)  
157 from the US Census Bureau (US Census Bureau, 2018).

158 The mean temperature during the campaign was 20.6 +/- 4.6 °C (mean +/- one standard deviation), which is 3-4°C  
159 warmer than the mean temperature during the 2009 PROPHET-CABINEX campaign (16.9 °C) (VanReken et al., 2015).  
160 Temperature conditions during this study are consistent with mean summertime temperatures from studies in 2008 and 2010  
161 (Toma and Bertman, 2012) and with historical mean temperature data for the month of July from the Pellston Regional  
162 Airport (Figure S1 in the Supplemental Information (SI)). The mean relative humidity (RH) during the campaign was 73.8  
163 +/- 17.5% , which is similar to conditions during the CABINEX campaign (74.5 +/- 17.5%) (VanReken et al., 2015). Winds  
164 recorded at the top of the PROPHET tower originated mostly from the west, southwest, and northwest (as shown in Figure  
165 S2 in the SI). The historical average precipitation according to the National Atmospheric Deposition Program (NADP)  
166 National Trends Network for the month of July from 1979-2015 for UMBS is 69.0 +/- 37.8 mm. During the PROPHET-  
167 AMOS 2016 campaign, the total accumulated precipitation was 79.0 mm, indicating that precipitation at the site during the  
168 campaign was within one standard deviation of the historical July average (NADP, 2016).

169 **2.2 Instrumentation and sampling**

170       A summary of the trace-gas measurements, instrumentation, and meteorological parameters on board the University of  
171 Houston/Rice University Mobile Air Quality Laboratory (MAQL) are summarized in Table S1 of the SI. Details and  
172 operation of the MAQL have been described previously in the literature (Leong et al., 2017; Wallace et al., 2018). The  
173 MAQL was situated approximately 10 meters to the east of the PROPHET tower. A photograph of the MAQL in stationary  
174 sampling mode is shown in Figure S3 in the SI. Table S2 in the SI lists the measurements, measurement methods, and  
175 sampling heights of other participating institutions at PROPHET-AMOS 2016 during the campaign. Measurements are  
176 reported in local time ([LT](#), Eastern Daylight Time (EDT)) during the campaign.

177 **2.2.1 Trace gases**

178       Below-canopy trace gases including nitric oxide (NO), nitrogen dioxide (NO<sub>2</sub>), total reactive nitrogen (NO<sub>y</sub>), O<sub>3</sub>, carbon  
179 monoxide (CO), and sulfur dioxide (SO<sub>2</sub>) were measured from a common inlet on the sampling arm of the MAQL. Reported  
180 values of nitrogen oxides (NO<sub>x</sub>) represent the sum of NO and NO<sub>2</sub>, while reported values of NO<sub>y</sub> include NO<sub>x</sub> and its  
181 reservoir species. These measurements were taken at a height of 6 m above ground level.

182 **2.2.2 HR-ToF-AMS**

183       The HR-ToF-AMS (Aerodyne Research Inc., USA) was used to measure non-refractory submicron particulate matter  
184 (NR-PM<sub>1</sub>) from the MAQL; measured composition includes OA, SO<sub>4</sub>, nitrate (NO<sub>3</sub>), ammonium (NH<sub>4</sub>), and chloride (Chl).  
185 Detailed descriptions of the operation and principles of the HR-ToF-AMS have been provided elsewhere (DeCarlo et al.,  
186 2007). In brief, particles are sampled through a 100-micron critical orifice and are focused into a particle beam using an  
187 aerodynamic lens. After traversing a vacuum chamber, the particles in the beam impact onto a tungsten vaporizer heated to  
188 600°C. The vapors formed are ionized by electron impact ionization at 70 eV. The resulting ions are detected using a high-  
189 resolution time-of-flight mass spectrometer. The HR-ToF-AMS was operated in a high mass sensitivity mode, referred to as  
190 V-mode. Ionization efficiency (IE) calibrations were performed at the beginning and end of the campaign using  
191 monodisperse 300 nanometer NH<sub>4</sub>NO<sub>3</sub> particles. Gas-phase interferences were subtracted from the data based on the  
192 observed signal when ambient air was sampled through a filter. Filter zeros were run each day at varying times of day.

193       Sampling was performed from the raised 6-m inlet on the common sampling arm of the MAQL (below canopy) and  
194 from a 30-m inlet on the PROPHET tower (above canopy). Copper tubing was used for the sampling inlets, and each inlet  
195 was fitted with cyclones to remove particles larger than 2.5 microns in diameter. Prior to the HR-ToF-AMS critical orifice,  
196 air was sampled through a nafion dryer to dry the sample flow. A three-way valve was used to alternate HR-ToF-AMS  
197 sampling between the above- and below-canopy inlets at 10-minute intervals.

198 **2.2.3 PTR-QiTof**

199       Above-canopy mixing ratios and fluxes, along with in-canopy vertical gradients, were measured for a wide array of  
200 VOCs during PROPHET-AMOS 2016 by Proton Transfer Reaction-Quadrupole interface Time-Of-Flight mass spectrometry  
201 (PTR-QiTof). A detailed description of the sampling configuration, calibration and zeroing procedures, humidity  
202 corrections, and instrumental performance during the campaign is provided by Alwe et al. (2019) and Millet et al. (2018).  
203 Briefly, six identical 45-m inlet lines (0.5" OD/0.375" ID PFA, each heated to 50°C) were installed on the PROPHET tower  
204 to sample from 34 m, 21 m, 17 m, 13 m, 9 m, and 5 m above ground level. Sample flow was maintained at ~40 standard  
205 L/min (SLM) for the 34 m inlet line and at >5-10 SLM for the others. Each hour, 30 min was spent sampling from the 34 m  
206 inlet to quantify above-canopy VOC mixing ratios and fluxes. The remainder of each hour was spent characterizing in-  
207 canopy vertical gradients by sequentially sampling from the other inlets (for 5 min apiece) followed by a 5-min instrumental  
208 blank.

## 209 2.3 HR-ToF-AMS data and positive matrix factorization analysis

210 Data analysis for HR-ToF-AMS data was performed in Igor Pro v6.37 using the SQUIRREL v1.57 (SeQUential Igor  
 211 data RetRiEvaL) and PIKA v1.16 (Peak Integration by Key Analysis) analysis toolkits. High-resolution mass spectral fitting  
 212 was performed on HR-ToF-AMS V-mode data. Ratios such as the oxygen-to-carbon elemental ratio (O:C) and hydrogen-to-  
 213 carbon elemental ratio (H:C) were determined according to the “improved-ambient” (IA) method (Canagaratna et al., 2015).  
 214 The IA method uses specific ion fragments to correct for compositional biases, and this method has been shown to calculate  
 215 accurately the elemental ratios of organic laboratory standards that are more representative of oxidized, ambient OA species  
 216 (Canagaratna et al., 2015). The default values for relative IE were used for each of the following species: OA (1.4),  $\text{SO}_4^{2-}$   
 217 (1.2),  $\text{NH}_4^+$  (4),  $\text{NO}_3^-$  (1.1), and Chl (1.3), where values in parentheses refer to the ratio of the IE of the given species with  
 218 respect to the value of IE of  $\text{NO}_3^-$  obtained during routine IE calibrations using  $\text{NH}_4\text{NO}_3$ .

To account for the effects of aerosol composition on the transmission efficiency of aerosols to the detection region of the HR-ToF-AMS, a chemical composition-dependent (and therefore time-dependent) collection efficiency (CDCE) was applied to the HR-ToF-AMS data (Middlebrook et al., 2012), which led to an campaign average CDCE of  $0.77 \pm 0.18$ . During the campaign, the HR-ToF-AMS time resolution was 40 seconds from 2 July 02:00 to 19 July 10:00 LT, after which the HR-ToF-AMS time resolution was changed to 30 seconds between 22 July 11:00 and 31 July 15:00 LT (due to instrumental changes after an HR-ToF-AMS power supply failure). Calculated detection limits of NR-PM<sub>1</sub> species are included in Table S3.

Positive matrix factorization (PMF) is a mathematical model in which measured data are decomposed into a combination of factors that have varying contributions throughout a time series. Here, the PMF model has been applied to HR-ToF-AMS data to retrieve OA factors that contain information regarding OA sources, chemical properties, and/or atmospheric processing (Jimenez et al., 2009; Ulbrich et al., 2009; Zhang et al., 2011). Subtypes of OA extracted from OA mass spectra using PMF often include (but are not limited to): more-oxidized oxygenated OA (MO-OOA), less-oxidized oxygenated OA (LO-OOA), hydrocarbon-like OA (HOA), biomass burning organic aerosol (BBOA), and cooking organic aerosol (COA) (Cubison et al., 2011; Jimenez et al., 2009; Mohr et al., 2012; Zhang et al., 2007, 2005). The OOA-related factors are generally considered to be associated with SOA, while subtypes such as HOA, BBOA, and COA are presumed to correspond to POA. Factors associated with isoprene-derived epoxydiol OA (IEPOX-OA) have also been identified using PMF using enhanced signals at  $m/z$  82 in their OA mass spectra (Hu et al., 2015). A detailed description of the PMF model (Paatero and Tapper, 1994; Paatero, 1997; Ulbrich et al., 2009; Xu et al., 2015) is included in the SI.

237 The results of the separate PMF analyses on above- and below-canopy OA are included in the SI. For the above-canopy  
 238 OA data, a summary of the PMF factor selection (Table S4), factor time series correlations with external data (Table S5),  
 239 factor mass spectra correlations with reference mass spectra (Table S6), time series of PMF model residuals (Figure S4), and  
 240 mass spectra and time series for possible two- to five-factor PMF solutions (Figure S5 - Figure S8) are shown in the SI.  
 241 VOCs measured above-canopy via PTR-QTOF at the top of the PROPHET tower are defined in Table S7, and factor time  
 242 series correlations with the time series of these VOCs are shown in Table S8. PMF diagnostics, such as the mass spectra and  
 243 time series correlation amongst factors (Figure S9), FPEAK and SEED diagnostic plots (Figure S10), results of the FPEAK  
 244 analysis (Table S9), model residual diagnostic plots (Figure S11), and results from bootstrapping analysis (Figure S12) are  
 245 shown in the SI. Finally, Figure S13 displays the time series and high-resolution mass spectra of the optimal solution for the  
 246 above-canopy OA dataset.

247 For the below-canopy OA data, a summary of the PMF factor selection (Table S10), factor time series correlations with  
 248 external data (Table S11), factor mass spectra correlations with reference mass spectra (Table S12), mass spectra and time  
 249 series of possible two- to five-factor PMF solutions (Figure S14 - Figure S17), factor time series correlations with VOCs  
 250 measured via PTR-QiToF at the 34-m inlet on the PROPHET tower (Table S13), mass spectra and time series correlations  
 251 amongst factors (Figure S18), FPEAK and SEED diagnostic plots (Figure S19), results from FPEAK analysis (Table S14  
 252 and Table S15), model residual diagnostic plots (Figure S20), and results from bootstrapping analysis (Figure S21) are

**Deleted:** EDT

**Deleted:** EDT

**Deleted:** Factorization of HR-ToF-AMS data follows the matrix form:  $\mathbf{A} = \mathbf{L} \mathbf{D} \mathbf{L}^T$

$X = GF + E \rightarrow \text{---} \rightarrow \text{---} \rightarrow \text{---} \rightarrow (1)^*$

where  $X$  is a  $m \times n$  matrix in which rows are the measured mass spectra at each time interval and columns are the time-varying signals of each sampled mass-to-charge ratio ( $m/z$ ).  $G$  is a  $m \times p$  matrix in which rows are the concentration time series for a given factor, and the number of factors (columns) in the solution is represented by  $p$ .  $F$  is a  $p \times n$  matrix in which  $p$  rows are the mass spectral profiles for a given factor. Finally,  $E$  is a  $m \times n$  matrix and contains the residuals not fit by the model at each time interval and sampled  $m/z$ . Using a least-squares algorithm, the values of  $G$  and  $F$  are determined by minimizing  $E$  using a quality of fit parameter ( $Q$ ) defined as the squared sum of the scaled residuals:<sup>1</sup>

In this study, PMF is applied separately to the above- and below-canopy HR-TOF-AMS OA high-resolution mass spectra between  $m/z$  12 and  $m/z$  115 using the generic 64-bit PMF2 v4.2 algorithm running in robust mode with a model error set to zero (Paatero, 1997; Paatero and Tapper, 1994; Ulbrich et al., 2009). The default PMF2 convergence criteria were used. The PMF Evaluation Tool v2.08 (PET) in Igor Pro v6.37 was used to treat the OA mass spectra error matrix, evaluate PMF output, and examine model statistics (Ulbrich et al., 2009). Organic isotopes were excluded from PMF analysis because isotope signals are scaled from their parent ions rather than being measured directly. A minimum error threshold was applied to the error matrix where any error values falling below this threshold are replaced. Variables (time series of  $m/z$  values) with a signal-to-noise ratio (SNR) less than 0.2 were removed, and variables with a SNR less than 2 were downweighted by a factor of 2. The error values for fragments such as  $O^+$ ,  $HO^+$ ,  $H_2O^+$ , and  $CO_2^+$  were also downweighted to avoid providing additional weight to the strong signal attributed to  $m/z$  44 in the default fragmentation table. To decrease the weight of each of these fragments, the error values for each of these fragment ions are all multiplied by a factor of 2 to appropriately downweight the  $m/z$  values related to  $m/z$  44.

Additionally, the error of the CHO' fragment was downweighted by multiplying the error value for this fragment by a factor of 4. Downweighting of CHO' was performed because  $m/z$  29 is a combination of signals from the CHO' ion ( $m/z$  29.0027) and a N<sub>2</sub> isotope ion ( $j15MN$ ,  $m/z$  29.0032). The close proximity of the CHO' and j15MN fragments ( $< 0.001$ ) using PIKA v1.16 likely causes the CHO' error to be underestimated (Xu et al., 2015).<sup>4</sup>

The optimal PMF solution for the OA data was determined by examining the following: (1) time series and mass spectra model residuals, (2) interpretability of factor diurnal variability, (3) [1]

385 shown in the SI. Finally, the time series and high-resolution mass spectra of the optimal three-factor solution for below-  
386 canopy OA are shown in Figure S22.

387 **2.4 HYSPLIT backward trajectory analysis**

388 **2.4.1 Trajectory cluster analysis**

389 Backward-trajectories are used in this study to determine the origin of air masses arriving at the field site using the  
390 Hybrid Single-Particle Lagrangian Integrated Trajectory (HYSPLIT) model (Draxler and Hess, 1998; Stein et al., 2015).  
391 Meteorological data from the US Eta data assimilation system archive at 40-km spatial resolution (EDAS40) are used for  
392 HYSPLIT trajectory calculations. The EDAS40 data output is constructed using forecasted data from the Eta model, which  
393 utilizes observations from surface, aircraft, and satellite data to predict meteorological parameters such as pressure, wind  
394 speed, and wind direction (Cooper et al., 2001).

395 In order to assess the influence of air mass histories on aerosols at each site, a cluster analysis was performed on  
396 backward trajectories using MeteoInfo v1.4.9R2 and the TrajStat v1.4.4R8 package (Wang, 2014; Wang et al., 2009). The  
397 angle distance clustering type is used in this study and calculates the angular distance between two backward trajectories as  
398 seen from the site, using methods outlined in Sirois and Bottemheim (1995). The number of suitable clusters is chosen based on  
399 the slope of the percentage change in total spatial variation versus number of clusters and a visual inspection of the mean  
400 trajectories of the cluster numbers.

401 **2.4.2 Weighted potential source contribution function (WPSCF) analysis**

402 In addition to a backward-trajectory cluster analysis performed for bulk aerosol properties and gas-phase species, two-  
403 day HYSPLIT backward-trajectories initiated from the PROPHET site at 500 m above ground level are used in a weighted  
404 potential source contribution function (WPSCF) analysis for OA factors. WPSCF analysis is performed in MeteoInfo  
405 v1.4.9R2 using the TrajStat v1.4.4R8 package and results are plotted using ESRI's ArcMap v10.1 (Wang, 2014; Wang et al.,  
406 2009). Similar PSCF analyses using backward-trajectories have been performed previously using aerosol properties (Bondy  
407 et al., 2017; Chang et al., 2017; Polissar, 1999; Schulze et al., 2018).

408 The number of backward-trajectory endpoints falling within a given grid cell with coordinates  $(i, j)$  is defined as  $n_{ij}$ .  
409 The number of instances in which backward-trajectories ending at a given grid cell have a value (i.e., OA factor mass  
410 concentration) higher than an arbitrarily set criterion value is defined as  $m_{ij}$ . The PSCF value for a cell at location  $(i, j)$  is  
411 then defined as follows:

$$412 PSCF_{ij} = \frac{m_{ij}}{n_{ij}} \quad (1)$$

413 When calculating values of PSCF, some grid cells will contain only a small number of backward-trajectory endpoints. In  
414 order to reduce the high uncertainties related to a limited number of endpoints falling within a grid cell in PSCF analysis, a  
415 weighting function is applied to the trajectory numbers following the methods of Polissar et al. (2001):

$$416 W_{ij} = \begin{cases} 1.00 & 80 < n_{ij} \\ 0.70 & 20 < n_{ij} \leq 80 \\ 0.42 & 10 < n_{ij} \leq 20 \\ 0.05 & n_{ij} \leq 10 \end{cases} \quad (2)$$

417 In this study, the domain of analysis is set to the geographical extents of the two-day HYSPLIT backward trajectories  
418 initiated from the PROPHET site. A grid cell size of  $0.5^\circ$  by  $0.5^\circ$  is used. Median values of the OA factors are used as the  
419 arbitrary criterion values. Overall, the WPSCF analysis allows for an identification of potential source areas, where higher  
420 WPSCF values within a region indicate a higher likelihood that this region results in observed values higher than the  
421 criterion values.

Deleted: 3

Deleted: 4

424 **2.5 Sonic anemometer data-processing**

425 Turbulence measurements during the campaign were obtained from five sonic anemometers installed on the PROPHET  
426 tower at the following measurement heights: 34m (CSAT 3B, Campbell Scientific Inc.), 29m (81000, RM Young), 21m  
427 (CSAT 3, Campbell Scientific Inc.), 13m (CSAT 3, Campbell Scientific Inc.), and 5m (CSAT 3, Campbell Scientific Inc.).  
428 The sonic anemometer at 34 m was operated continuously during the campaign while data are only available from the lower  
429 heights from 9 July – 29 July 2016. High-frequency data are de-spiked (data points outside of 3.5-standard deviations are  
430 removed) and then separated into 30-minute windows to apply a tilt correction such that the x-axis is rotated into the  
431 direction of the mean wind velocity (Foken, 2008). Reynolds decomposition is then applied to the three-dimensional wind  
432 components ( $u, v, w$ ), so each variable (e.g.,  $u$ ) is separated into its mean ( $\bar{u}$ ) and fluctuating component ( $u'$ ). The friction  
433 velocity,  $u^*$ , is defined then as

$$434 u^* = -\bar{u}' \bar{w}' \quad (3)$$

435 Any 30-minute periods that experienced rain (as measured by the rain-gauge at the UMBS AmeriFlux tower), weak winds  
436 (winds less than  $0.5 \text{ m s}^{-1}$  at the top sonic anemometer), or wind directed through the tower were excluded due to potential  
437 interference.

**Deleted:** 9<sup>th</sup>, 2016

**Deleted:** 29<sup>th</sup>,

**Deleted:** 5

438 **3 Results and discussion**

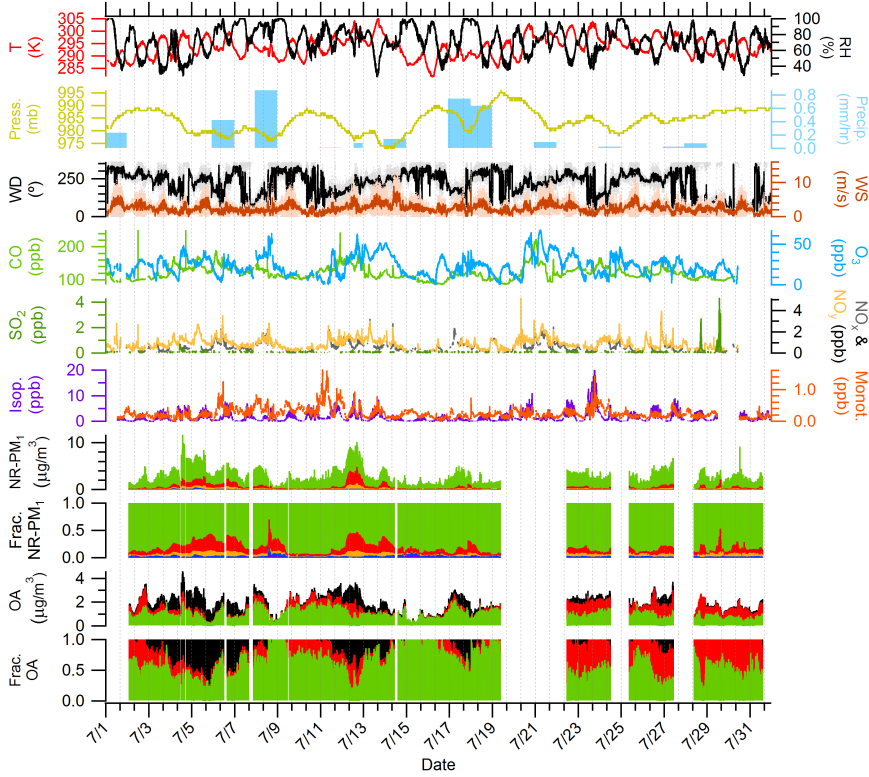
439 **3.1 Backward-trajectory cluster analysis**

440 Two-day backward trajectories are initiated from the PROPHET site and calculated at one-hour intervals from the  
441 beginning to the end of the campaign (1 July 00:00 – 31 July 21:00 ~~LT~~) at 500 meters above ground level, an elevation  
442 selected to be within the boundary layer during the day and to avoid trajectory interaction with the surface. A total of 742  
443 two-day backward-trajectories are calculated over the course of the campaign. Cluster analysis resulted in three directional  
444 clusters: southerly (299 of 742), northeasterly (192 of 742), and northwesterly (251 of 742) (as shown in Figure S23 in the SI  
445 as Cluster 1, 2, and 3 respectively). Further description of cluster number selection is discussed in Figure S24 in the SI.  
446 Similar to the air mass history analyses at the PROPHET site in Cooper et al. (2001) and VanReken et al. (2015), eight-hour  
447 transitional periods between backward-trajectory classifications were removed from analysis because it is likely that the  
448 chemical species from these different air masses are mixed. In total, transitional periods composed 22% of the total number  
449 of backward-trajectories (165 of 742 total), and the remaining 577 are used for further analysis. Mean values of  
450 anthropogenically-influenced species such as  $\text{SO}_4$  and benzene were not statistically significantly different ( $p < 0.01$ )  
451 between trajectories from northeasterly and northwesterly clusters, so trajectories from these two clusters are grouped to  
452 represent a “northerly” air mass type. During the PROPHET-AMOS study, northerly transport occurred during 60% of the  
453 study period (341 of 577), while southerly transport occurred 40% of the time (236 of 577). This type of air-mass  
454 classification is consistent with previous summertime studies at the PROPHET site where northerly transport occurred 44%  
455 (1998), 60% (2009), and 57% (2014) of the time and southerly transport occurred 24% (1998), 29% (2009), and 43% (2014)  
456 of the time (Cooper et al., 2001; Gunsch et al., 2017; VanReken et al., 2015).

**Deleted:** EDT

457 **3.2 Non-refractory submicron time series and bulk chemical composition**

458 Figure 1 shows the time series of the mass concentrations of OA,  $\text{SO}_4$ ,  $\text{NH}_4$ ,  $\text{NO}_3$ , and Chl as measured by the HR-ToF-  
459 AMS. Mass concentrations plotted in Figure 1 represent time series data from both the above- and below-canopy sampling  
460 inlets. The average total NR-PM<sub>1</sub> (sum of mass concentrations of OA,  $\text{SO}_4$ ,  $\text{NH}_4$ ,  $\text{NO}_3$ , and Chl) is  $2.3 \pm 1.5 \mu\text{g m}^{-3}$ . High  
461 NR-PM<sub>1</sub> concentration episodes (7/3-7/7 and 7/11-7/14) are strongly influenced by southerly air masses advecting



466  
467 Figure 1: Overview of time series of the following from top to bottom: temperature (T) and RH; pressure (Press.)  
468 and precipitation (Precip.); wind direction (WD) and wind speed (WS); CO and O<sub>3</sub>; SO<sub>2</sub>, NO<sub>x</sub>, and NO<sub>y</sub>; isoprene  
469 (Isop.) and total monoterpenes (Monot.); particulate OA (green), NO<sub>3</sub> (blue), SO<sub>4</sub> (red), NH<sub>4</sub> (orange), and Chl  
470 (purple); fraction of species to total NR-PM<sub>1</sub>, OA factors derived from PMF, and fractional contribution of OA  
471 factors to total OA. OA factors are colored as follows: MO-OOA (black), IEPOX-OA (red), and 91Fac (green).  
472 Precipitation data are provided from the NADP site in Cheboygan County, MI. Trace gas data (CO, O<sub>3</sub>, SO<sub>2</sub>, NO<sub>x</sub>,  
473 and NO<sub>y</sub>) are measured from the 6-m inlet on the MAQL. Meteorological data (T, RH, Press., WD, and WS) and  
474 VOC data (Isop. and Monot.) are measured from the 34-m inlet on the PROPHET tower. The OA time series include  
475 data from both heights (6 m and 30 m), with the sampling switched at 10-minute intervals.

Formatted: Font: (Default) Times New Roman, Bold

476 to the site, as confirmed by the HYSPLIT backward-trajectory clusters shown in Figure S23 in the SI. Northerly backward-  
477 trajectories originated over clean, remote areas in Canada, while southerly backward-trajectories originated over more  
478 anthropogenically influenced areas. OA is the dominant NR-PM<sub>1</sub> component over the entire campaign, representing

480 approximately 84.2% of the NR-PM<sub>1</sub> mass. SO<sub>4</sub> contributes the second highest average mass fraction to NR-PM<sub>1</sub> (10.7%)  
481 followed by NH<sub>4</sub> (3.1%), NO<sub>3</sub> (1.6%), and Chl (0.4%). During periods of northerly flow, OA represents 89.5% of the  
482 average NR-PM<sub>1</sub> mass, while SO<sub>4</sub>, NH<sub>4</sub>, NO<sub>3</sub> and Chl represent 6.9%, 1.9%, 1.3%, and 0.4%, respectively. Periods of  
483 southerly flow decrease the relative contribution of OA to 75.5% and Chl to 0.3% while increasing the relative contribution  
484 of SO<sub>4</sub> to 16.8%, NH<sub>4</sub> to 5.6%, and NO<sub>3</sub> to 1.3%. The increased fractional contribution of OA during periods of northerly-  
485 originating air is consistent with results from VanReken et al. (2015), who found that water-soluble organics dominated  
486 aerosol mass during periods of “clean” northerly flow at the PROPHET site. Sheesley et al. (2004) also found the aerosol  
487 organic carbon composition at a remote site in the upper peninsula of Michigan (approximately 100 miles from the  
488 PROPHET site) was greatly influenced by the source region of the air parcel. This study found that both stagnant and  
489 northerly air parcels contained higher concentrations of pinonic acid and limited amounts of primary emission tracer  
490 compounds, while anthropogenically influenced air parcels from the south and northwest contained higher concentrations of  
491 aromatic and aliphatic dicarboxylic acids.

492 Diurnal plots for OA, SO<sub>4</sub>, NH<sub>4</sub>, NO<sub>3</sub>, O:C, and H:C are shown in Figure S25 in the SI. The diurnal profiles of OA,  
493 SO<sub>4</sub>, and NH<sub>4</sub> are all relatively flat and do not have a clear diurnal trend. The lack of clear diurnal variations for SO<sub>4</sub> is  
494 consistent with regional transport as the source of SO<sub>4</sub> during this campaign. The diurnal variations of NO<sub>3</sub> show increases  
495 in the morning, with a maximum around approximately 10:00 local time, and lower concentrations in the afternoon.

496 Using the backward-trajectory clustering results described in Section 3.1, mean values of NR-PM<sub>1</sub>, NR-PM<sub>1</sub> species, OA  
497 elemental ratios, meteorological parameters, and trace gases for the entire campaign, northerly, and southerly backward-  
498 trajectory clusters are shown in Table 1. Overall, relative to northerly air masses, southerly air masses were found to be  
499 warmer (~2 °C), more humid (~5%), and associated with higher concentrations of NO<sub>x</sub>, NO<sub>y</sub>, O<sub>3</sub>, and benzene. Furthermore,  
500 on average, southerly air masses had higher concentrations of NR-PM<sub>1</sub>, OA, SO<sub>4</sub>, NH<sub>4</sub>, and NO<sub>3</sub>. Higher levels of OA  
501 oxidation (8% difference) based on O:C are also observed during periods of southerly flow (O:C = 0.69 versus 0.75 for  
502 northerly versus southerly flow, respectively). An additional metric of oxidation, the oxidation state of carbon (OSc),  
503 indicates that the degree of oxidation is higher during periods of southerly flow (OSc = -0.12 versus 0.06 for northerly versus  
504 southerly flow, respectively, where OSc = 2 \* O:C - H:C) (Kroll et al., 2011). The factor of 5 differences between northerly  
505 and southerly SO<sub>4</sub> is consistent with the increased influence of SO<sub>2</sub> point sources from electric-generating units south of the  
506 site in Ohio, Indiana, and Illinois. Overall, these observations demonstrate that anthropogenic influence from southerly flow  
507 directly affects NR-PM<sub>1</sub> mass concentrations, NR-PM<sub>1</sub> composition, the degree of OA oxidation, and trace gas mixing ratios  
508 at this site. Results are in agreement with VanReken et al. (2015), where southerly air masses or those “anthropogenically  
509 impacted” were found to contain higher aerosol loadings (in terms of aerosol volume, particle number, and median particle  
510 diameter) and hygroscopicity, along with increased trace gases abundances, as compared to northerly air masses or “clean”  
511 regimes.

512 Oxygen-containing ion families (C<sub>x</sub>H<sub>y</sub>O<sub>z+1</sub><sup>+</sup>) represent over 50% of the campaign-averaged OA high-resolution mass  
513 spectrum, and this high degree of oxygenation is reflected in an average O:C ratio of 0.71 +/- 0.08 and an average H:C ratio  
514 of 1.49 +/- 0.06. A distinct peak at m/z 44 in the average mass spectrum accounts for 14.1% of the total OA. The peak at  
515 m/z 44 is mainly composed of the CO<sub>2</sub><sup>+</sup> ion (96.0% of m/z 44). The ratio of m/z 44 to the total signal in the organic mass  
516 spectrum (f<sub>44</sub>), a surrogate for O:C and an indicator for photochemical aging, in this study is 0.14. Together with the average  
517 O:C ratio (0.71) observed in this study, these values are consistent with OOA observed across AMS datasets (Jimenez et al.,  
518 2009; Ng et al., 2010). Other prominent ions in the campaign-averaged high-resolution mass spectrum include m/z 55, 82,  
519 and 91. Fragments at m/z 55 represent 2.4% of the total OA, and are representative of both oxygenated and hydrocarbon  
520 fragments, such as C<sub>3</sub>H<sub>5</sub>O<sup>+</sup> (50.2% of m/z 55) and C<sub>4</sub>H<sub>7</sub><sup>+</sup> (42.9% of m/z 55). The possible OA sources leading to increased  
521 signal at m/z 82 (0.46% of total OA) and 91 (0.62% of total OA) will be discussed in the following section. Figure S25 in  
522 the SI shows the diurnal variations of O:C and H:C, indicating relatively stable diurnal cycles. Increases in H:C are observed  
523 starting at 9:00 before reaching a maximum at midday (13:00) followed by a slow decrease between the hours of 13:00 and  
524 20:00, while an opposite pattern is observed for mean values of O:C.

525

526 **Table 1: Campaign-averaged values (+/- one standard deviation from the mean) of mass concentrations of NR-PM<sub>1</sub>, VOC and**  
 527 **trace gas mixing ratios, and meteorological parameters, as well as hourly-averaged values associated with northerly and southerly**  
 528 **backward-trajectory clusters. Northerly and southerly air masses are defined in Section 3.1 using a cluster analysis of HYSPLIT**  
 529 **two-day backward trajectories.**

Parameter	Campaign	Northerly	Southerly
NR-PM <sub>1</sub> (µg m <sup>-3</sup> )	2.3 ± 1.5	1.8 ± 0.7	3.6 ± 2.0
OA (µg m <sup>-3</sup> )	1.9 ± 1.0	1.6 ± 0.6	2.6 ± 1.3
SO <sub>4</sub> (µg m <sup>-3</sup> )	0.3 ± 0.4	0.1 ± 0.1	0.7 ± 0.6
NH <sub>4</sub> (µg m <sup>-3</sup> )	0.1 ± 0.1	0.04 ± 0.04	0.2 ± 0.2
NO <sub>3</sub> (µg m <sup>-3</sup> )	0.04 ± 0.03	0.02 ± 0.01	0.06 ± 0.05
Chl (µg m <sup>-3</sup> )	0.01 ± 0.00	0.01 ± 0.00	0.01 ± 0.00
O:C	0.7 ± 0.1	0.7 ± 0.1	0.8 ± 0.1
H:C	1.5 ± 0.1	1.5 ± 0.0	1.4 ± 0.00
OSc	-0.1 ± 0.2	-0.1 ± 0.1	0.1 ± 0.2
Isoprene (ppb) <sup>a,b</sup>	1.6 ± 1.9	1.5 ± 1.5	1.8 ± 1.5
Monoterpenes (ppb) <sup>a,b</sup>	0.3 ± 0.2	0.2 ± 0.1	0.2 ± 0.2
Benzene (ppb) <sup>a</sup>	0.04 ± 0.02	0.03 ± 0.01	0.05 ± 0.02
NO (ppt) <sup>c</sup>	24.1 ± 36.4	21.5 ± 16.2	29.7 ± 29.5
NO <sub>2</sub> (ppt) <sup>c</sup>	593.0 ± 445.8	369.4 ± 257.7	872.0 ± 478.6
NO <sub>y</sub> (ppt) <sup>c</sup>	934.5 ± 490.0	610.5 ± 271.8	1283.9 ± 412.6
O <sub>3</sub> (ppb) <sup>c</sup>	24.1 ± 11.9	20.1 ± 8.3	30.5 ± 13.2
CO (ppt) <sup>c</sup>	120.6 ± 21.5	109.6 ± 12.6	134.7 ± 21.7
SO <sub>2</sub> (ppb) <sup>b,c</sup>	31.3 ± 174.2	45.0 ± 212.0	23.1 ± 64.2
Temperature (°C) <sup>c</sup>	20.6 ± 4.6	20.3 ± 4.5	22.4 ± 4.5
Relative Humidity (%) <sup>c</sup>	73.8 ± 17.3	68.6 ± 17.0	73.5 ± 17.6

530 <sup>a</sup> VOC measurements using University of Minnesota's PTR-QiToF from the 34-m inlet on the PROPHEt tower.

531 <sup>b</sup> Table entries where the differences between the northerly and southerly backward-trajectories mean values are not  
 532 statistically significant ( $p < 0.01$ ) using a two-sample t-test.

533 <sup>c</sup> Trace gas and meteorological parameters measured from onboard the MAQL.

534

### 535 3.3 Organic aerosol source apportionment

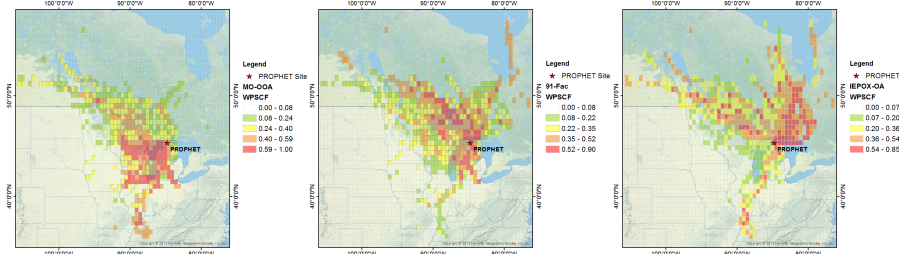
536 A three-factor solution is obtained for both the above-canopy inlet at 30 meters above the UMBS forest floor (A-MO-  
 537 OOA, A-IPEOX-OA, A-91Fac) and the below-canopy inlet at 6 meters within the UMBS canopy (B-MO-OOA, B-IPEOX-  
 538 OA, and B-91Fac). The 91Fac factor represents OA with enhanced signal at m/z 91 in the mass spectrum. The addition of  
 539 more factors to the PMF solution beyond three factors resulted in less physically meaningful and interpretable factors. Thus,  
 540 the three-factor solution is considered the optimal solution for the above- and below-canopy OA datasets. In this study, seed  
 541 = 0 was chosen for both PMF solutions as there was minimal variation in  $Q/Q_{exp}$  across the 50 seeds. Solutions at FPEAK =  
 542 0 were chosen because solutions at other FPEAK values did not present improved correlations between factors and reference  
 543 mass spectra.

544 Time series of mass concentrations and time series of fractional contributions to total OA are shown in Figure 1. The  
 545 O:C ratio of each of the OA factors are as follows: 0.65 (IPEOX-OA), 0.71 (91Fac), and 0.89-0.90 (MO-OOA), all of which  
 546 indicate the high degree of oxygenation in each of the factors. For the above-canopy PMF solution, 91Fac makes the largest

547 contribution to the total OA (43.8%), followed by IEPOX-OA (32.8%) and MO-OOA (23.4%). For the below-canopy PMF  
 548 solution, 91Fac also makes the largest contribution to the total OA (42.5%), followed by IEPOX-OA (34.0%) and MO-OOA  
 549 (23.5%). Details on the chemical composition, mass spectral characteristics and diurnal profiles of each factor are discussed  
 550 further in the SI.

551 Hourly averages of the above-canopy OA factors are paired with hourly two-day backward-trajectories for WPSCF  
 552 analysis. Results from WPSCF analysis using above-canopy OA data (Figure 2) indicate that A-MO-OOA predominantly  
 553 originates from southerly air masses, as supported by external measurements data such as benzene, OVOCs, carbonyls, and  
 554  $\text{SO}_4$ . Air masses that originate from the south pass over the large urban centers of Chicago, Milwaukee, and Detroit. This  
 555 further supports the aged, transported nature and anthropogenic influences of the observed A-MO-OOA at this site. In  
 556 contrast, no strong indication of a distinct source region is observed for 91Fac. This could suggest a more localized source  
 557 of 91Fac in relation to the site. Combining these WPSCF results with correlations of 91Fac with VOC masses corresponding  
 558 to monoterpene oxidation suggests that 91Fac is sourced from local biogenic, monoterpene-oxidation related chemistry (Xu  
 559 et al., 2018). Finally, WPSCF results for A-IEPOX-OA indicate that this OA factor coincides with more northerly airflow  
 560 with some contributions from northwesterly flow. These northerly source regions driving A-IEPOX-OA correspond to more  
 561 rural, less anthropogenically influenced locations in Canada. Interestingly, an instance of high WPSCF values for A-  
 562 IEPOX-OA and A-MO-OOA can be traced back to areas near the southeastern tip of Missouri and western Tennessee,  
 563 implying long-range transport of these OA factors. Backward-trajectories associated with this instance of high WPSCF  
 564 values for IEPOX-OA pass over areas in the high isoprene-emitting region in the Ozarks of southern Missouri, which is  
 565 commonly referred to as the “isoprene volcano” (Carlton and Baker, 2011; Wiedinmyer et al., 2005). The median mass  
 566 concentrations of above-canopy OA factors used as the criterion values for the WPSCF method were A-MO-OOA:  $0.31 \mu\text{g m}^{-3}$   
 567 A-91Fac:  $0.68 \mu\text{g m}^{-3}$ , and A-IEPOX-OA:  $0.58 \mu\text{g m}^{-3}$ . Overall, WPSCF analysis indicates that transport from southerly  
 568 flow (A-MO-OOA), local sources (A-91Fac), and transport from northerly flow (A-IEPOX-OA) are related to the OA  
 569 factors observed at this site.

570

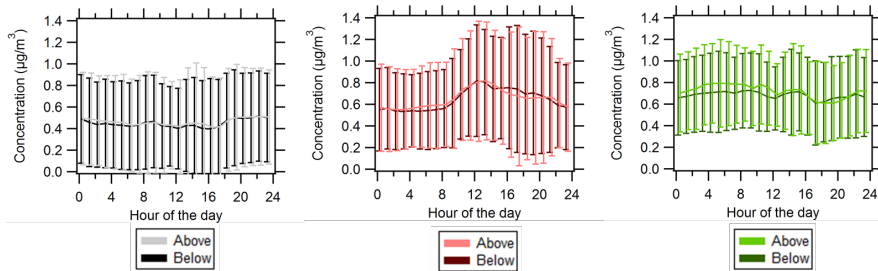


571  
 572 **Figure 2: WPSCF backward-trajectory analysis maps for the following hourly-averaged OA factors from left to right: above-**  
 573 **canopy MO-OOA, above-canopy 91Fac and above-canopy IEPOX-OA. The geographical location of the PROPHET site is**  
 574 **represented by a red star. WPSCF analysis is performed using HYSPLIT two-day backward trajectories, a grid cell size of  $0.5^\circ$  by**  
 575  **$0.5^\circ$ , and the geographical domain of the extents of the two-day backward trajectories. Median mass concentrations of above-**  
 576 **canopy OA factors (A-MO-OOA:  $0.31 \mu\text{g m}^{-3}$ , A-91Fac:  $0.68 \mu\text{g m}^{-3}$ , and A-IEPOX-OA:  $0.58 \mu\text{g m}^{-3}$ ) are used as the criterion**  
 577 **WPSCF values. Color scales correspond to probability of source regions for each respective OA factor, and it should be noted that**  
 578 **the range and gradation of the color scale changes between each plot.**

579

580 Overall, PMF analysis for both sampling inlets at the site indicates that the OA is a combination of MO-OOA, 91Fac,  
 581 and IEPOX-OA. The dominant OA factor is 91Fac, and during periods of southerly flow MO-OOA contributes relatively  
 582 more (time series of the fractional contributions to total OA shown from both inlets is shown in Figure 1 and is also shown

583 separately for each inlet in Figure S13 and Figure S22 in the SI). On average, source apportionment results indicate that the  
 584 OA at both inlets generally had similar average fractional OA contributions and degrees of oxidation. Diurnal profiles for  
 585 above- and below-canopy OA are shown in Figure 3 and indicate that diurnal profiles and variations are similar between the  
 586 two inlets for each OA factor. It is worth noting the diurnal pattern of the IEPOX-OA factor, likely indicating a relatively  
 587 small influence of local isoprene emissions.  
 588



589  
 590 **Figure 3: Diurnal profiles of (left) MO-OOA, (middle) IEPOX-OA, and (right) 91Fac where solid lines represent average values  
 591 and whiskers represent one standard deviation from the mean. Darker colors represent below-canopy OA (B-MO-OOA, B-  
 592 IEPOX-OA, B-91Fac) while lighter colors represent above-canopy OA (A-MO-OOA, A-IEPOX-OA, A-91Fac). Data for below-  
 593 canopy OA factors have been offset by 15 minutes simply to aid plot interpretation.**

594

### 595 3.4 Vertical characterization of above- and below-canopy NR-PM<sub>1</sub> and OA factors

#### 596 3.4.1 Similarity between above- and below-canopy environments

597 Mean values of NR-PM<sub>1</sub>, NR-PM<sub>1</sub> species, OA elemental ratios, meteorological parameters, VOCs, and trace gases from  
 598 the above- and below-canopy inlets are summarized in Table 2. Each of the mean values for the parameters listed in Table 2  
 599 are within one standard deviation of each other for the below- and above-canopy sampling heights. However, results from  
 600 Wilcoxon rank-sum tests indicate that the medians for a majority of the above- and below-canopy parameters are  
 601 significantly different ( $p = 0.05$ ). To provide a comparison of the two inlets on the same time scale, scatter plots of 30-  
 602 minute averaged values are shown in Figure 4 for OA factors, total OA, SO<sub>4</sub>, and O:C. For reference, a 1:1 line is shown on  
 603 each scatter plot. Values falling within one standard deviation are similar between above and below canopy, while values  
 604 deviating farther from the 1:1 line indicate values in which the above- or below-canopy environment had differing  
 605 concentrations. Figure 4 illustrates that mass concentrations of OA factors, total OA, and SO<sub>4</sub> were similar over a majority  
 606 of the campaign and suggests that the above- and below-canopy environments were generally coupled from a PM  
 607 perspective. It also appears that total OA, MO-OOA, IEPOX-OA, and 91Fac show increases above canopy relative to below  
 608 canopy at the highest end of the range of the measurements.

609 Results from a recent study from the PROPHET-AMOS 2016 campaign by Millet et al. (2018) indicate that flux of  
 610 isoprene and monoterpenes at the canopy-atmosphere boundary represents over half of the net carbon flux, while OVOCs  
 611 constitute a majority of the species with detectable VOC fluxes. Overall, the authors report that the observed and modeled  
 612 net carbon flux during the campaign was upward (canopy emission) during the campaign in 2016. Additionally, in-canopy  
 613 gradients of directly emitted BVOCs, such as isoprene and monoterpenes, indicate patterns that are consistent with their  
 614 respective temperature, light, and physical emission dependencies (higher concentrations in-canopy for isoprene and higher

615 in the lower canopy for monoterpenes). On the other hand, in-canopy gradients of secondary products from BVOC  
616 oxidation, such as acetic acid and glycoaldehyde, indicate patterns consistent with net nighttime uptake and a weak peak

617

618 **Table 2: Campaign-averaged values (+/- one standard deviation) of mass concentrations of NR-PM<sub>1</sub>, VOC and trace gas mixing**

619 ratios, and meteorological parameters above and below the canopy.

Parameter <sup>a, b</sup>	Above	Below
NR-PM <sub>1</sub> ( $\mu\text{g m}^{-3}$ )	2.4 $\pm$ 1.6	2.3 $\pm$ 1.5
OA ( $\mu\text{g m}^{-3}$ )	1.9 $\pm$ 1.0	1.8 $\pm$ 1.0
SO <sub>4</sub> ( $\mu\text{g m}^{-3}$ )	0.3 $\pm$ 0.5	0.3 $\pm$ 0.4
NH <sub>4</sub> ( $\mu\text{g m}^{-3}$ )	0.1 $\pm$ 0.2	0.1 $\pm$ 0.2
NO <sub>x</sub> ( $\mu\text{g m}^{-3}$ )	0.04 $\pm$ 0.04	0.04 $\pm$ 0.03
Chl ( $\mu\text{g m}^{-3}$ )	0.01 $\pm$ 0.00	0.01 $\pm$ 0.00
O:C	0.7 $\pm$ 0.1	0.7 $\pm$ 0.1
H:C <sup>c</sup>	1.5 $\pm$ 0.1	1.5 $\pm$ 0.1
OSc	0.0 $\pm$ 0.2	-0.1 $\pm$ 0.2
Isoprene (ppb)	1.6 $\pm$ 1.9	1.8 $\pm$ 2.2
Monoterpenes (ppb)	0.3 $\pm$ 0.2	0.3 $\pm$ 0.3
Benzene (ppb)	0.04 $\pm$ 0.02	0.04 $\pm$ 0.02
NO (ppt)	36.0 $\pm$ 56.9	24.1 $\pm$ 36.4
NO <sub>2</sub> (ppt)	564.8 $\pm$ 393.2	593.0 $\pm$ 448.8
O <sub>3</sub> (ppb)	32.2 $\pm$ 12.2	24.1 $\pm$ 11.9
Temperature (°C) <sup>c</sup>	20.7 $\pm$ 4.1	20.6 $\pm$ 4.6
Relative Humidity (%)	71.5 $\pm$ 17.3	73.8 $\pm$ 17.3

620 <sup>a</sup> Summary statistics for NR-PM<sub>1</sub> measurements were calculated using 5-minute averaged data, VOC measurements using 1-  
621 minute averaged data (University of Minnesota's PTR-QiTof 5-m inlet and 34-m inlet), NO<sub>x</sub> above-canopy measurements  
622 using 5-minute averaged data (University of Toronto), NO<sub>x</sub> and O<sub>3</sub> below-canopy measurements using 5-minute averaged  
623 data (MAQL), and O<sub>3</sub> 1-minute averaged data (CU-Boulder's 27-m inlet on the AmeriFlux Tower).

624 <sup>b</sup> Percent of data below detection limit for NR-PM<sub>1</sub>: NH<sub>4</sub> (4% / 4%) and Chl (59% / 63%), VOCs: isoprene (30% / 30%),  
625 monoterpenes (56% / 36%), benzene (100% / 100%), and NO (37% / 22%), where percentages are shown for above- and  
626 below-canopy data, respectively. Unless otherwise stated, the percentage below detection limit for all other parameters is  
627 0%.

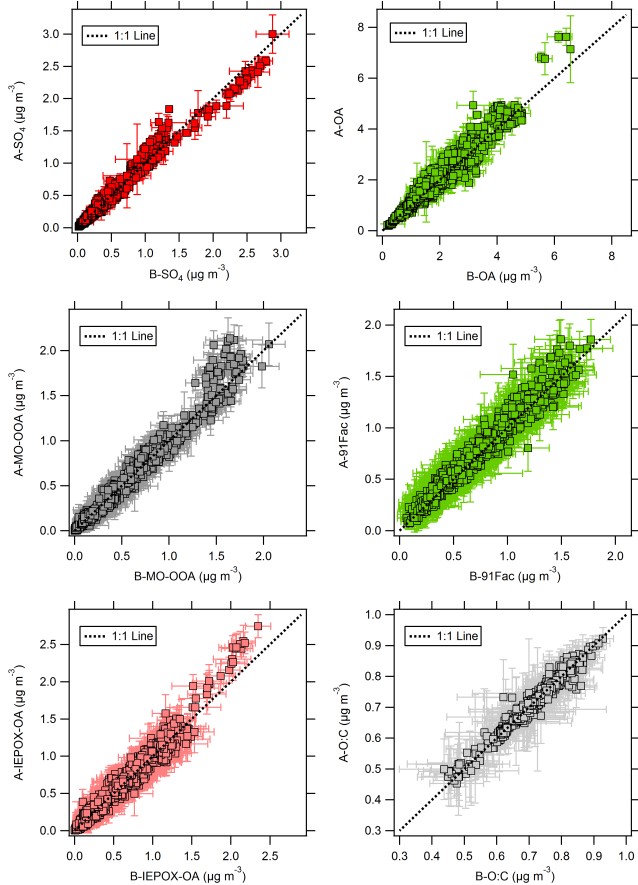
628 <sup>c</sup> Table entries where the null hypothesis ("equal medians") between the above- and below-canopy data cannot be rejected  
629 and was not statistically significant ( $p > 0.05$ ) using a two-sided, non-parametric Wilcoxon rank-sum test. All other table  
630 entries indicate that the null hypothesis ("equal medians") can be rejected at the statistical significance level ( $p < 0.05$ ).

631 concentration near the mid-canopy. Correlation analysis of these secondary oxidation products and HCOOH indicates that  
632 HCOOH likely originates from a secondary source in this environment (Alwe et al., 2019). In the present study, the overall  
633 homogeneity in OA factors implies that, despite vertical gradients in trace gases and BVOCs from primary emission and  
634 secondary production, turbulent mixing of aerosols between the forest canopy and the atmosphere is efficient.

635 Furthermore, this similarity between the above- and below-canopy environments suggests that the chemical timescales  
636 of SOA formation processes likely are long relative to residence times due to turbulent mixing (Foken et al., 2012), assuming  
637 relatively constant background levels. Ultimately, the observed similarity agrees with previous modeling work that predicts  
638 similar SOA mass loadings at these two heights (Ashworth et al., 2015; Schulze et al., 2017). The results shown in the  
640 present work also are in agreement with measurements at the site in 2009, showing that aerosol gradients on the PROPHET

641 tower "existed at times between the above-canopy (31.4m) and understory environments (5 m)," but that the understory  
 642 conditions were generally similar to that of the above-canopy conditions (VanReken et al., 2015). The vertical similarity in  
 643

644



645

646

647 **Figure 4: Scatter plots of above- (A) and below- (B) canopy hourly-averaged values for: (top from left to right)  $SO_4$   
 648 and total OA, (middle from left to right) MO-OOA and 91Fac, and (bottom) IEPOX-OA and campaign O:C. The  
 649 three-way valve switched between the two inlets at 10-minute intervals, so 30-minute averaged mass concentrations  
 650 allows for a comparison of both inlets on the same time basis. Above-canopy values are plotted on the y-axis of each  
 651 plot and below-canopy values are plotted on the x-axis of each plot. Averages are shown with squares; whiskers**

652 represent one standard deviation from the mean. For reference, a 1:1 line is shown with each plot. Outliers on the  
653 O:C plot corresponding to periods of precipitation were removed.

654  
655 NR-PM<sub>1</sub> is also in agreement with findings in the Amazon forest, where a balance between upward and downward fine  
656 particle fluxes was found (Rizzo et al., 2010) and in a southeast Asian rainforest, where PM<sub>1</sub> did not show significant  
657 variations with height during the daytime (Whitehead et al., 2010).

#### 658 3.4.2 Episodes of vertical differences in NR-PM<sub>1</sub>

659 Episodes of vertical differences in NR-PM<sub>1</sub> between the two inlets were observed, and four such episodes are described  
660 here: Episode #1 (Period: 7/3/2016 19:30 to 7/5/2016 15:00 LT), Episode #2 (11 July 15:00 to 12 July 23:00 LT), Episode  
661 #3 (7/16/2016 21:30 to 7/19/2016 08:30 LT), and Episode #4 (7/26/2016 08:30 to 7/31/2016 13:30 LT). Episodes were  
662 defined as sustained periods in which a vertical difference in OA or SO<sub>4</sub> was greater than or equal to concentrations  
663 representing  $\geq 25\%$  of the campaign averaged OA or SO<sub>4</sub>. The “vertical difference,” symbolized as  $\Delta$  in Figure 5, is defined  
664 as the difference between above- and below-canopy values, where the positive convention indicates larger concentrations  
665 above the canopy. Episodes #1, #3, and #4 indicate increased above-canopy OA concentrations, while Episode #2 indicates  
666 increased below-canopy SO<sub>4</sub> concentrations. Episodes with higher above-canopy NR-PM<sub>1</sub> ranged up to  $\sim 1.0 \mu\text{g m}^{-3}$  higher  
667 in OA and  $\sim 0.5 \mu\text{g m}^{-3}$  higher in SO<sub>4</sub> relative to equivalent above/below mass ( $A = 0$ ). Figure 5 shows time series of vertical  
668 differences in OA factors and SO<sub>4</sub> and estimates of friction velocity ( $u^*$ ) at five different heights (not equal to those for the  
669 VOC measurements) on the PROPHET tower over the campaign. Calculated from three-dimensional wind velocity data,  $u^*$   
670 is a function of the shear stress at the surface and is used in this study as a metric of in-canopy mixing (Equation 5).▼

671 The sum of the delta values for each OA factor ( $\Sigma\Delta\text{OA}$  Factors) for the episodes are shown in Figure 6, with  
672 corresponding observations of  $u^*$  and vertical differences in SO<sub>4</sub> and O<sub>3</sub>. Figure 6 shows that vertical differences in OA  
673 correlate with vertical differences in SO<sub>4</sub> for Episodes #1 and #4, while  $\Sigma\Delta\text{OA}$  Factors during Episode #3 coincides with  
674 higher above-canopy O<sub>3</sub> concentrations. Correlations between chemical species for Episode #2 are weaker. Correlation  
675 coefficients ( $r$ ) for each episode are 0.69 (Episode #1  $\Sigma\Delta\text{OA}$  Factors-Sulfate), -0.44 (Episode #2 Sulfate- $u^*$ ), 0.34 (Episode  
676 #3  $\Sigma\Delta\text{OA}$  Factors-Ozone), and 0.59 (Episode #4  $\Sigma\Delta\text{OA}$  Factors-Sulfate). These episodes have different OA factor  
677 composition: MO-OOA contributing a larger percentage during Episode #1 and #2, 91Fac contributing roughly half in  
678 Episode #3, and IEPOX-OA contributing more than half of the total OA vertical difference in Episode #4.▲

#### 679 3.5 The role of mixing and particulate SO<sub>4</sub> in vertical differences in OA

680 The diurnal profile of vertical difference episodes for total OA, SO<sub>4</sub>, and OA factors in 2016 indicate there is no clear  
681 diurnal pattern observed for any of these species (Figure S26 in the SI). Maximum vertical differences for SO<sub>4</sub>, total OA,  
682 and MO-OOA are observed around 3PM. For total OA, a gradual increase occurs at 9AM before reaching a maximum  
683 vertical difference at 3PM, suggesting that the episodes of higher above-canopy NR-PM<sub>1</sub> begin shortly after the most  
684 common observed hours of canopy uncoupling from the site in 2009. The initiation of these events may also be attributed to  
685 venting of the nocturnal boundary layer as it breaks up in the morning hours, as observed for events of upward particle  
686 number fluxes by Whitehead et al. (2010).

687 To assess the agreement between the occurrence of episodes and micrometeorological measurements of in-canopy  
688 mixing, episode-specific data for Episodes #2-4 are shown in Figure 6. During Episode #1,  $u^*$  data are available only at  
689 36m, so no friction velocity data are shown, preventing a full analysis similar to those performed for the other three episodes.  
690 However, based on similarity in sulfate enhancements, it can be assumed that Episode #1 is somewhat similar to Episode #4.

691 During Episode #2, based on the backward trajectory cluster analysis shown in Table 1 and the WPSCF results, regional  
692 transport is the likely source of the PM, including the enhancements below canopy. Prior to this episode, SO<sub>4</sub> and MO-OOA  
693 are uniform from below-to-above canopy. The below-canopy enhancement then reaches up to  $0.3 \mu\text{g m}^{-3}$  of SO<sub>4</sub>.

**Deleted:** EDT

**Deleted:** 11

**Deleted:** 12

**Deleted:** EDT

**Deleted:** EDT

**Deleted:** EDT

**Deleted:** 1

**Deleted:** The “vertical difference,” symbolized as  $\Delta$  in Figure 5, is defined as the difference between above- and below-canopy values, where the positive convention indicates larger concentrations above the canopy. ...

**Formatted:** Font: (Default) Times New Roman

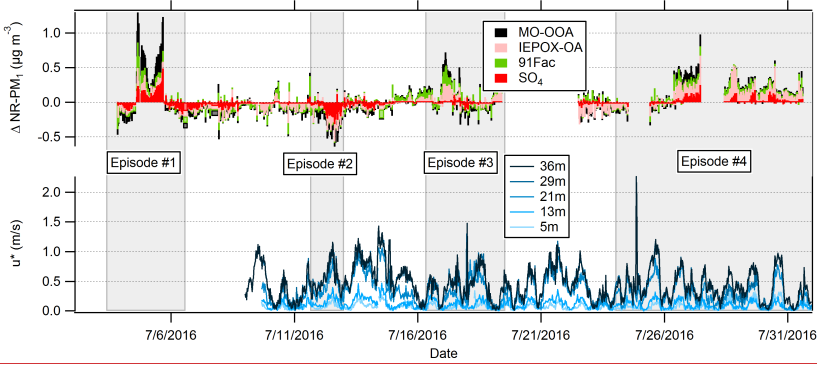
**Deleted:** Episodes of total OA factor vertical difference ( $\Sigma\Delta\text{OA}$  Factors) are shown in Figure 6...

**Formatted:** Font: (Default) Times New Roman

**Formatted:** Font: (Default) Arial, Font color: Text 1

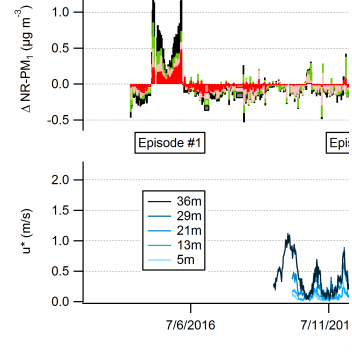
**Deleted:** temporal

708 Downmixing of clean air from aloft could lead to lower concentrations above canopy, meaning that the observed difference  
 709 would be caused by decreasing above-canopy concentrations, not increasing below-canopy concentrations. However,  
 710 below-canopy concentrations are observed to increase while above-canopy concentrations decrease. Without a local, below-  
 711 canopy source, this indicates that pollutants from above canopy are mixed into the below-canopy region at a rate faster than  
 712 they are lost to deposition. Regional pollutants, advected to the site above the boundary layer, can be mixed down to the  
 713 surface with daytime boundary layer growth, as has been found in previous aircraft campaigns (Berkowitz et al., 1998;  
 714 Thorberry et al., 2001). Downward transport of air masses from the surrounding region has also been hypothesized to  
 715 contribute to higher ratios of organic nitrogen to organic carbon ratios in water-soluble aerosols within a forest canopy  
 716 relative to its forest floor (Miyazaki et al., 2014).

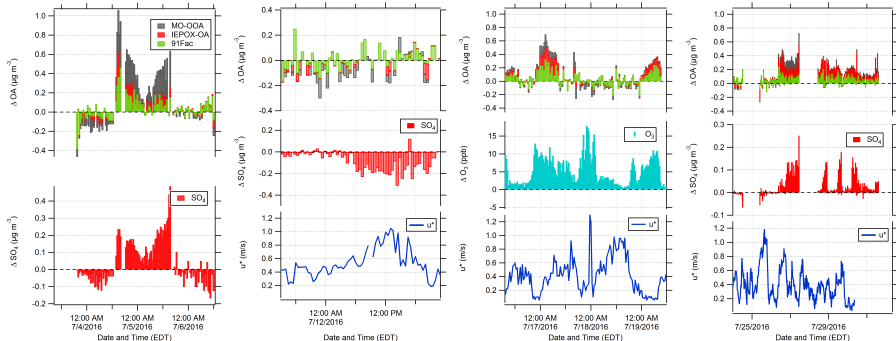


717  
 718 **Figure 5:** Time series of (top) observed NR-PM<sub>1</sub> vertical differences between above- and below-canopy inlets and  
 719 (bottom) friction velocity ( $u^*$ ) in m/s at five different heights on the PROPHET tower. Vertical differences are  
 720 defined as  $\Delta$  Species, where  $\Delta$  refers to the Above-Canopy minus the Below-Canopy mass concentration. Note that  
 721 the elevations for  $u^*$  are slightly different than those for trace gas sampling.  
 722

723 During Episodes #3 and #4, periods of above-canopy enhancement in OA factors coincide with relatively lower  $u^*$  ( $u^* <$   
 724 0.2 m/s during Episode #3 and  $u^* < 0.6$  m/s during Episode #4, with the average  $u^*$  considering all heights over the duration  
 725 of the episode), with lower friction velocities and greater above-canopy enhancement in Episode 3. In the case of Episode  
 726 #3, lower in-canopy mixing, mostly occurring during nighttime, agrees well with periods of higher above-canopy OA factor  
 727 and O<sub>3</sub> concentrations. In this case, both IEPOX-OA and 91Fac contribute to the OA enhancement, likely due to strong  
 728 photochemistry both locally and during transport (as indicated by increased O<sub>3</sub>). Episode #4 is the longest duration episode;  
 729 however, the agreement between low-mixing and above-canopy PM enhancements is more variable during this case. Similar  
 730 to Episode #3, the lowest values of friction velocity occur during the nighttime or early morning. Despite the temporal  
 731 misalignment of  $\Delta$ OA and low  $u^*$ , it should be noted that friction velocities lower than the campaign average ( $\sim 0.4$  m/s) are  
 732 observed during the latter periods of Episode #4 (7/28-7/30), which is consistent with the low mixing hypothesis presented  
 733 for Episode #3. Therefore, it appears that stagnant conditions above the canopy created an environment where canopy  
 734 exchange became limited and air masses did not fully penetrate into the canopy; aerosol deposition below canopy potentially  
 735 enhanced the positive delta values. This scenario could also promote in-canopy OA accumulation, but this does not appear  
 736 to have occurred, implying that other factors contributed to these vertical differences. Instead, it appears that increased  
 737 sulfate loading was associated with this transport and that this increased sulfate above the canopy led to enhancements above



739 canopy, particularly of IEPOX-OA relative to 91Fac, as shown in Figure 6. This also could be related to associated changes  
740 in aerosol liquid water.  
741



742 **Figure 6: Time series of observed NR-PM vertical difference episodes: (from left to right) Episode #1, Episode #2,**  
743 **Episode #3, and Episode #4.** Data shown for Episode #1, Episode #2, and Episode #4 include vertical differences in  
744 30-minute averaged above- and below-canopy  $\text{SO}_4$ , while data shown for Episode #3 show vertical differences in 30-  
745 minute averaged above- and below-canopy  $\text{O}_3$ . The  $\text{O}_3$  data were measured from the AmeriFlux Tower at 6 meters  
746 and 27 meters and were provided courtesy of CU-Boulder. Friction velocity measurements at 29m on the PROPHET  
747 tower are also provided for Episodes #2-4.

748 The probability distributions of  $\Delta \text{SO}_4$  and  $\Delta \text{O}_3$  between episodes and the average for the entire PROPHET campaign are  
749 compared in Figure S27 of the SI. The cumulative distribution function (CDF) for  $\Delta \text{SO}_4$  indicates that Episodes #1 and #4  
750 had higher probabilities of positive  $\Delta \text{SO}_4$  (denoting higher above-canopy concentrations), while Episode #2 had higher  
751 probabilities of negative  $\Delta \text{SO}_4$  (denoting higher below-canopy concentrations). The episode-specific CDFs for #1 and #2 are  
752 also different from the total campaign CDF, implying that the vertical differences observed were distinct events. The  
753 average  $\text{O}_3$  difference between the 6- and 27-m inlets on the AmeriFlux tower throughout the campaign indicated that  $\text{O}_3$   
754 was on average 5 ppb greater at the 27-m inlet, with the difference reaching as high as 34 ppb on 6 July and 20 July. The  
755 probability distribution of vertical  $\text{O}_3$  differences observed during Episode #3 is markedly different than those observed  
756 during Episode #1, Episode #4, and the remainder of the campaign. This indicates that  $\text{O}_3$  had a larger probability of being  
757 between 0-10 ppb higher above the canopy during this episode compared to the rest of the campaign.

758 Based on Episode #1 and Episode #4, one of several potential driving factors of vertical differences for OA is a vertical  
759 difference in particulate  $\text{SO}_4$ . Figure 7 indicates the vertical differences in OA and  $\text{SO}_4$  relative to their respective above-  
760 canopy concentrations. This metric is defined as "% PM Difference," where PM is the given PM constituent and is equal to  
761 the  $\Delta \text{PM}$  constituent divided by the above-canopy PM concentration. Data that fall in the upper right and bottom left  
762 quadrants correspond to higher above- and higher below-canopy concentrations, respectively. The vertical difference above  
763 or below the canopy can be up to approximately 35% of the total available  $\text{SO}_4$  or OA at the site. Figure 7 indicates that  
764 there is a strong linear relationship between the % $\text{SO}_4$  Difference and %OA Difference during the campaign, even outside of  
765 the Episodes defined here.

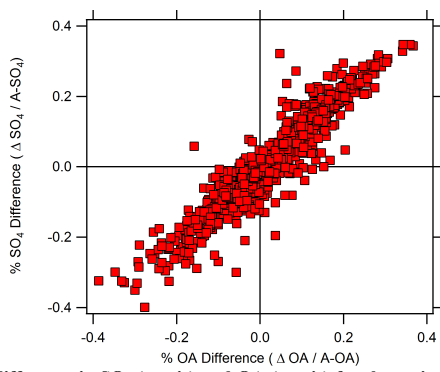
766 The concurrent features of vertical differences in OA factors and  $\text{SO}_4$  observed in Episodes #1, #2, and #4 and OA  
767 factors and  $\text{O}_3$  in Episode #3 suggest that long-range regional transport (enhanced MO-OOA,  $\text{SO}_4$ , and/or  $\text{O}_3$ ) is a key first  
768 step in causing these differences. Local through-canopy mixing then determines whether the enhancement is above

**Deleted:** 6

**Deleted:** 20

**Deleted:** a

774 (Episodes #1, #3, and #4) or below (Episode #2) the canopy. The transported material can then impact local chemistry.  
 775 Increased  $\text{SO}_4$  likely increases aerosol hygroscopicity resulting in increased ALW, which could result in increased  
 776 partitioning of semi-volatile organics to the condensed phase (i.e., IEPOX-OA) (Budisulistiorini et al., 2017; El-Sayed et al.,  
 777 2018; Marais et al., 2016). Pre-existing OA (i.e., MO-OOA) transported with  $\text{SO}_4$  aerosol could also play a role in the  
 778 partitioning of OA above the canopy during these episodes. Vertical gradients in  $\text{O}_3$  coinciding with Episode #3 (higher  $\text{O}_3$   
 779 above) could initiate relatively local formation of extremely low volatility compounds, which are first-generation oxidation  
 780 products of  $\alpha$ -pinene and  $\text{O}_3$  (Jokinen et al., 2015). Based on the WPSCF and backward trajectory clustering results, cooler,  
 781 northerly air masses associated with IEPOX-OA also could promote partitioning of semi-volatile organics to the particle  
 782 phase. It is important to note that it is difficult to conclude the exact chemical mechanisms that are influencing these events  
 783 due to their low mass loadings and episodic nature and the consistently higher above-canopy  $\text{O}_3$  concentrations during the  
 784 campaign.  
 785



786  
 787 **Figure 7: Scatter plot of % difference in  $\text{SO}_4$  (y-axis) and OA (x-axis) for the entire campaign. The % difference is**  
 788 **calculated as  $\Delta$  Species / Above-Canopy Species concentration, and is representative of the normalized  $\Delta$  Species**  
 789 **concentration.**

790  
 791 Understanding these events is important because uncoupled forest-canopy conditions have been observed in a number of  
 792 locations (Foken et al., 2012; Whitehead et al., 2010) and could indicate differences between above-canopy and surface level  
 793 PM. One-dimensional modeling has revealed that the timescales of turbulent transport inside a forest canopy can be much  
 794 shorter (minutes) than the timescale of aerosol dynamics and deposition (hours) (Rannik et al., 2016), but this evaluation  
 795 suggests that advective episodes can cause vertical gradients that are not locally driven. Above-canopy OA and particle  
 796 fluxes have been observed in other studies (Farmer et al., 2013; Pryor et al., 2007), suggesting the need for careful evaluation  
 797 of whether differences are driven by local chemistry, long-range transport, or a combination thereof.  
 798

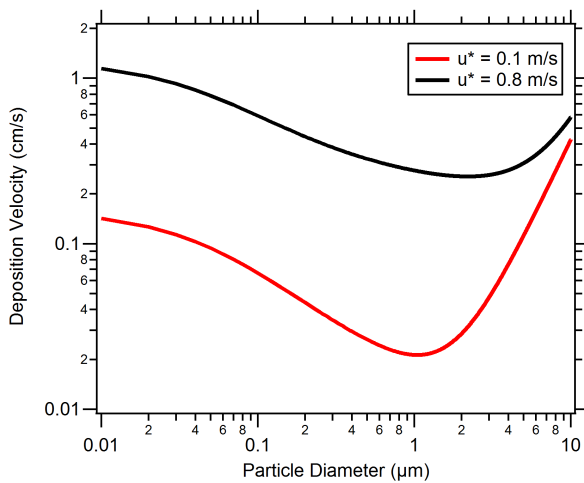
### 799 3.6 Particle dry deposition model

800 To investigate broadly the effects of canopy mixing on particle deposition in a forest canopy, a particle dry deposition  
 801 model is used. Note that we are not applying this through the canopy but to illustrate the relationship between deposition  
 802 and  $u^*$ . The resistance model for particle dry deposition assumes that the deposition process is controlled by three  
 803 resistances in series: aerodynamic, quasi-laminar, and canopy resistance (Seinfeld and Pandis, 2006). Details on the particle

804 dry deposition model are included in the SI. Conditions and parameters representative of the land use category, season, and  
805 forest canopy present at the PROPHET site are used as model inputs.

806 Figure 8 displays model results for deposition velocity as a function of particle diameter under stable atmospheric  
807 conditions. For illustration, test cases are shown for  $u^*$  values for low in-canopy mixing ( $u^* = 0.1 \text{ m/s}$ ) and high in-canopy  
808 mixing ( $u^* = 0.8 \text{ m/s}$ ). Values of  $u^*$  were chosen based on the range of  $u^*$  values observed during the campaign at 29m on  
809 the PROPHET tower. For the submicron particle diameter range (0.1 to 1 micron), a characteristic minimum in deposition  
810 velocity is observed for both test cases at 1 micron diameter. Deposition modeling indicates that higher deposition velocities  
811 are achieved in the high in-canopy mixing test case, implying that there is less canopy transport resistance to the surface and  
812 more deposition in the canopy. This corresponds to Episode #2.

813

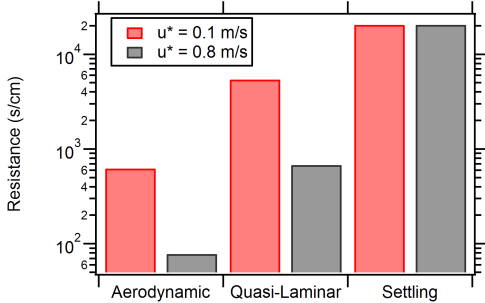


814 **Figure 8: Particle dry deposition velocity resistance model results plotted by particle diameter and friction velocity.**  
815 Two test cases of low and high friction velocity, representative of data collected at the PROPHET site, are plotted in  
816 red and black solid lines, respectively. Land-use conditions and seasonal parameters similar to the PROPHET  
817 campaign were used as inputs to the particle dry deposition model. Additional model parameters are provided in the  
818 SI.

820

821 Deposition modeling also indicates relatively lower deposition velocities for the low mixing condition test case, which  
822 suggests that particles aloft are transported less efficiently into the forest (similar to the conditions present for Episodes #3  
823 and #4). A comparison of the deposition resistances (shown in Figure 9) indicates that aerodynamic and quasi-laminar  
824 resistances in the low-mixing test case are an order of magnitude greater than the high-mixing case. The settling removal  
825 resistance is the same between both test cases because it is merely a function of diameter. A greater aerodynamic resistance  
826 limits turbulent transport from the above-canopy layer to the surface layer and greater quasi-laminar layer resistance limits  
827 transport to just above the surface by lowering particle impaction. In total, this result emphasizes the importance of in-  
828 canopy transport and mixing in governing particle concentrations in forests.

829



830  
 831 **Figure 8: Deposition and particle settling (accounts for the effect of sedimentation) resistances comparison for low  
 832 and high friction velocities. Resistance comparison assumes a 1 micron particle diameter.**

Deleted: 9

833 **4 Conclusions**

834 In this study, source apportionment of OA using separate PMF analyses on inlets situated above and below a forest  
 835 canopy resulted in three OA factors at a site in northern Michigan. Similarity in OA composition, concentration, and diurnal  
 836 profiles was observed between the two inlets, suggesting that turbulent transport efficiently mixes OA across the canopy.  
 837 However, OA factor vertical differences between the two inlets were observed during four separate episodes. During these  
 838 episodes, vertical differences were both positive (greater concentrations above the canopy) and negative (greater  
 839 concentrations below canopy). NR-PM<sub>1</sub> composition amongst these episodes was unique (Episode #1: MO-OOA dominant,  
 840 Episode #2: SO<sub>4</sub> dominant, Episode #3: 91Fac dominant, Episode #4: IEPOX-OA dominant). Furthermore, the vertical  
 841 difference concentrations can be 35% of the total available SO<sub>4</sub> or OA at the site. It has also been shown that relative  
 842 vertical differences in SO<sub>4</sub> and OA are linearly associated, suggesting the role of regional SO<sub>4</sub> in vertical profiles of NR-PM<sub>1</sub>  
 843 in forested environments.

844 Using micrometeorological measurements, it has been [shown in this work](#) that periods of low in-canopy mixing  
 845 conditions can be associated with the timing of vertical difference episodes where above-canopy concentrations are larger  
 846 than those below. The opposite scenario is hypothesized to be associated with transport of air from aloft or with  
 847 accumulation of material below canopy more rapidly than it is deposited. Either way, these results suggest that canopy  
 848 mixing impacts particle levels. However, under low-mixing scenarios, it appears that enhancements as defined here depend  
 849 on both these conditions and the presence of transported O<sub>3</sub> or SO<sub>4</sub> to enhance IEPOX-OA and 91Fac levels.

Deleted: hypothesized

850 To the knowledge of the author, this is one of only a few studies that have assessed vertical profiles in OA factors  
 851 above and below a forest canopy, and the first study to observe episodes of vertical differences in OA factors above and  
 852 below a forest canopy. This work adds to the existing literature on aerosol chemistry in a forest canopy environment  
 853 presented by Rizzo et al. (2010) and Whitehead et al. (2010) and to literature on vertical profiles of OA in an urban  
 854 environment by Özturk et al. (2013).

855 To investigate the effects of forest canopies on SOA formation, small-scale models, such as those described in  
 856 Schulze et al. (2017) and Ashworth et al. (2015), have been developed. The OA data from this work can be used to validate  
 857 such models and are particularly relevant to these modeling efforts, as the models were developed using campaign data from  
 858 the PROPHET site in 2009. Vertical transport and horizontal advection are both sources of uncertainty in current forest  
 859 canopy-atmosphere exchange models, which are designed to focus on local processes. Ultimately, the vertical similarity in

862 NR-PM<sub>1</sub> OA composition observed in this study implies that it may be valid to assume that below-canopy OA composition  
863 is generally representative of the OA composition in the atmospheric layer directly above the canopy and vice versa.  
864 However, this work highlights that advection of regional pollution into forested regions can lead to in-canopy gradients that  
865 are not present under purely local conditions.  
866

#### 867 **Data Availability**

868 Data are available through contacting the corresponding author.

#### 869 **Author Contributions**

870 A.A.T.B. prepared the manuscript with input from all authors. A.A.T.B., H.W.W. and R.J.G. conceived of the study and  
871 operated and analyzed the data from the HR-ToF-AMS. S.K. and A.L.S. investigated friction velocity and in-canopy  
872 mixing. H.D.A. and D.B.M. collected and analyzed VOC data. J.H.F., M.H.E. and S.A. collected and analyzed trace gas  
873 data and operated the MAQL.

#### 874 **Competing Interests**

875 The authors declare they have no conflict of interest.

#### 876 **Acknowledgements**

877 The assistance of all staff and collaborators at UMBS is gratefully acknowledged. We would like to thank Wei Wang at  
878 University of Colorado Boulder for assistance in collecting O<sub>3</sub> data at the AmeriFlux tower and the Murphy group at the  
879 University of Toronto for provision of nitrogen oxide data. This work was funded by the National Science Foundation  
880 (NSF) under grant AGS-1552086. PTR-QiToF measurements during PROPHET-AMOS were also supported by NSF (grants  
881 AGS-1428257+AGS-1148951). Trace gas and meteorological measurements on board the MAQL were also supported by  
882 NSF (grant AGS-1552077).

#### 883 **References**

884 Alwe, H.D., Millet, D.B., Chen, X., Raff, J.D., Payne, Z.C., Fledderman, K., 2019. Oxidation of Volatile Organic  
885 Compounds as the Major Source of Formic Acid in a Mixed Forest Canopy. *Geophysical Research Letters* 0.  
886 <https://doi.org/10.1029/2018GL081526>

887 Ashworth, K., Chung, S.H., Griffin, R.J., Chen, J., Forkel, R., Bryan, A.M., Steiner, A.L., 2015. FORest Canopy  
888 Atmosphere Transfer (FORCAST) 1.0: a 1-D model of biosphere-atmosphere chemical exchange. *Geoscientific  
889 Model Development* 8, 3765–3784. <https://doi.org/10.5194/gmd-8-3765-2015>

890 Baldocchi, D., Guenther, A.B., Harley, P., Klinger, L., Zimmerman, P., Lamb, B., Westberg, H., 1995. The fluxes and air  
891 chemistry of isoprene above a deciduous hardwood forest. *Philosophical Transactions: Physical Sciences and  
892 Engineering* 351, 279–296.

893 Bergen, K.M., Dronova, I., 2007. Observing succession on aspen-dominated landscapes using a remote sensing-ecosystem  
894 approach. *Landscape Ecology* 22, 1395–1410. <https://doi.org/10.1007/s10980-007-9119-1>

895 Berkowitz, C.M., Fast, J.D., Springston, S.R., Larsen, R.J., Spicer, C.W., Doskey, P.V., Hubbe, J.M., Plastridge, R., 1998.  
896 Formation mechanisms and chemical characteristics of elevated photochemical layers over the northeast United  
897 States. *J. Geophys. Res.* 103, 10631–10647. <https://doi.org/10.1029/97JD03751>

898 Bondy, A.L., Wang, B., Laskin, A., Craig, R.L., Nhliziyo, M.V., Bertman, S., Pratt, K.A., Shepson, P.B., Ault, A.P., 2017.  
899 Inland Sea Spray Aerosol Transport and Incomplete Chloride Depletion: Varying Degrees of Reactive Processing  
900 Observed during SOAS. *Environ. Sci. Technol.* <https://doi.org/10.1021/acs.est.7b02085>

901 Brown, S.S., Osthoff, H.D., Stark, H., Dubé, W.P., Ryerson, T.B., Warneke, C., de Gouw, J.A., Wollny, A.G., Parrish, D.D.,  
902 Fehsenfeld, F.C., Ravishankara, A.R., 2005. Aircraft observations of daytime NO<sub>x</sub> and N<sub>2</sub>O<sub>x</sub> and their implications  
903 for tropospheric chemistry. *Journal of Photochemistry and Photobiology A: Chemistry* 176, 270–278.  
904 <https://doi.org/10.1016/j.jphotochem.2005.10.004>

905 Bryan, A.M., Bertman, S.B., Carroll, M.A., Dusant, S., Edwards, G.D., Forkel, R., Griffith, S., Guenther, A.B., Hansen,  
906 R.F., Helmgig, D., Jobson, B.T., Keutsch, F.N., Lefer, B.L., Pressley, S.N., Shepson, P.B., Stevens, P.S., Steiner,  
907 A.L., 2012. In-canopy gas-phase chemistry during CABINEX 2009: sensitivity of a 1-D canopy model to vertical  
908 mixing and isoprene chemistry. *Atmospheric Chemistry and Physics* 12, 8829–8849. <https://doi.org/10.5194/acp-12-8829-2012>

910 Budisulistiorini, S.H., Nenes, A., Carlton, A.G., Surratt, J.D., McNeill, V.F., Pye, H.O.T., 2017. Simulating Aqueous-Phase  
911 Isoprene-Epoxydiol (IEPOX) Secondary Organic Aerosol Production During the 2013 Southern Oxidant and  
912 Aerosol Study (SOAS). *Environmental Science & Technology* 51, 5026–5034.  
913 <https://doi.org/10.1021/acs.est.6b05750>

914 Canagaratna, M.R., Jimenez, J.L., Kroll, J.H., Chen, Q., Kessler, S.H., Massoli, P., Hildebrandt Ruiz, L., Fortner, E.,  
915 Williams, L.R., Wilson, K.R., Surratt, J.D., Donahue, N.M., Jayne, J.T., Worsnop, D.R., 2015. Elemental ratio  
916 measurements of organic compounds using aerosol mass spectrometry: characterization, improved calibration, and  
917 implications. *Atmospheric Chemistry and Physics* 15, 253–272. <https://doi.org/10.5194/acp-15-253-2015>

918 Carlton, A.G., Baker, K.R., 2011. Photochemical Modeling of the Ozark Isoprene Volcano: MEGAN, BEIS, and Their  
919 Impacts on Air Quality Predictions. *Environmental Science & Technology* 45, 4438–4445.  
920 <https://doi.org/10.1021/es200050x>

921 Carroll, M.A., Bertman, S.B., Shepson, P.B., 2001. Overview of the Program for Research on Oxidants: PHotochemistry,  
922 Emissions, and Transport (PROPHET) summer 1998 measurements intensive. *Journal of Geophysical Research*  
923 106.

924 Chang, Y., Deng, C., Cao, F., Cao, C., Zou, Z., Liu, S., Lee, X., Li, J., Zhang, G., Zhang, Y., 2017. Assessment of  
925 carbonaceous aerosols in Shanghai, China – Part 1: long-term evolution, seasonal variations, and meteorological  
926 effects. *Atmos. Chem. Phys.* 17, 9945–9964. <https://doi.org/10.5194/acp-17-9945-2017>

927 Cooper, O.R., Moody, J.L., Thornberry, T.D., Town, M.S., Carroll, M.A., 2001. PROPHET 1998 meteorological overview  
928 and air-mass classification. *Journal of Geophysical Research* 106.

929 Cubison, M.J., Ortega, A.M., Hayes, P.L., Farmer, D.K., Day, D., Lechner, M.J., Brune, W.H., Apel, E., Diskin, G.S.,  
930 Fisher, J.A., Fuelberg, H.E., Hecobian, A., Knapp, D.J., Mikoviny, T., Riemer, D., Sachse, G.W., Sessions, W.,  
931 Weber, R.J., Weinheimer, A.J., Wisthaler, A., Jimenez, J.L., 2011. Effects of aging on organic aerosol from open  
932 biomass burning smoke in aircraft and laboratory studies. *Atmospheric Chemistry and Physics* 11, 12049–12064.  
933 <https://doi.org/10.5194/acp-11-12049-2011>

934 DeCarlo, P.F., Kimmel, J.R., Trimborn, A., Northway, M.J., Jayne, J.T., Aiken, A.C., Gonin, M., Fuhrer, K., Horvath, T.,  
935 Docherty, K.S., others, 2006. Field-deployable, high-resolution, time-of-flight aerosol mass spectrometer.  
936 *Analytical Chemistry* 78, 8281–8289.

937 Ditto, J.C., Barnes, E.B., Khare, P., Takeuchi, M., Joo, T., Bui, A.A.T., Lee-Taylor, J., Eris, G., Chen, Y., Aumont, B.,  
938 Jimenez, J.L., Ng, N.L., Griffin, R.J., Gentner, D.R., 2018. An omnipresent diversity and variability in the chemical  
939 composition of atmospheric functionalized organic aerosol. *Communications Chemistry* 1, 75.  
940 <https://doi.org/10.1038/s42004-018-0074-3>

941 Draxler, R.R., Hess, G.D., 1998. An overview of the HYSPLIT\_4 modeling system for trajectories, dispersion, and  
942 deposition. *Australian meteorological magazine* 47.

943 El-Sayed, M.M.H., Ortiz-Montalvo, D.L., Hennigan, C.J., 2018. The effects of isoprene and NO<sub>x</sub> on secondary organic  
944 aerosols formed through reversible and irreversible uptake to aerosol water. *Atmospheric Chemistry and Physics*  
945 18, 1171–1184. <https://doi.org/10.5194/acp-18-1171-2018>

946 Farmer, D.K., Chen, Q., Kimmel, J.R., Docherty, K.S., Nemitz, E., Artaxo, P.A., Cappa, C.D., Martin, S.T., Jimenez, J.L.,  
947 2013. Chemically Resolved Particle Fluxes Over Tropical and Temperate Forests. *Aerosol Science and Technology*  
948 47, 818–830. <https://doi.org/10.1080/02786826.2013.791022>

949 Fehsenfeld, F.C., Calvert, J.G., Fall, R., Goldan, P., Guenther, A., Hewitt, C.N., Lamb, B., Shaw, L., Trainer, M., Westberg,  
950 H., Zimmerman, P., 1992. Emissions of volatile organic compounds from vegetation and the implications for  
951 atmospheric chemistry. *Global Biogeochemical Cycles* 6.

952 Finnigan, J., 2000. Turbulence in plant canopies. *Annual Review of Fluid Mechanics* 32, 519–571.

953 Foken, T., Meixner, F.X., Falge, E., Zetzsch, C., Serafimovich, A., Bargsten, A., Behrendt, T., Biermann, T., Breuninger, C.,  
954 Dix, S., Gerken, T., Hunner, M., Lehmann-Pape, L., Hens, K., Jocher, G., Kesselmeier, J., Lüers, J., Mayer, J.-C.,  
955 Moravek, A., Plake, D., Riederer, M., Rütz, F., Scheibe, M., Siebicke, L., Sörgel, M., Staudt, K., Trebs, I.,  
956 Tsokankunku, A., Welling, M., Wolff, V., Zhu, Z., 2012. Coupling processes and exchange of energy and reactive  
957 and non-reactive trace gases at a forest site – results of the EGER experiment. *Atmospheric Chemistry and Physics*  
958 12, 1923–1950. <https://doi.org/10.5194/acp-12-1923-2012>

959 Fuentes, J.D., Wang, D., Bowling, D.R., Potosnak, M., Monson, R.K., Goliff, W.S., Stockwell, W.R., 2007. Biogenic  
960 Hydrocarbon Chemistry within and Above a Mixed Deciduous Forest. *Journal of Atmospheric Chemistry* 56, 165–  
961 185. <https://doi.org/10.1007/s10874-006-9048-4>

962 Gao, W., Wesely, M.L., Doskey, P.V., 1993. Numerical modeling of the turbulent diffusion and chemistry of NO<sub>x</sub>, O<sub>3</sub>,  
963 isoprene, and other reactive trace gases in and above a forest canopy. *Journal of Geophysical Research: Atmospheres* 98, 18339–18353. <https://doi.org/10.1029/93JD01862>

964 Geron, C., Rasmussen, R., R. Arnts, R., Guenther, A., 2000. A review and synthesis of monoterpene speciation from forests  
965 in the United States. *Atmospheric Environment* 34, 1761–1781. [https://doi.org/10.1016/S1352-2310\(99\)00364-7](https://doi.org/10.1016/S1352-2310(99)00364-7)

966 Goldstein, A.H., Galbally, I.E., 2007. Known and unexplored organic constituents in the earth's atmosphere. *Environmental  
967 Science & Technology*.

968 Gordon, M., Staebler, R.M., Liggio, J., Vlasenko, A., Li, S.-M., Hayden, K., 2011. Aerosol flux measurements above a  
969 mixed forest at Borden, Ontario. *Atmospheric Chemistry and Physics* 11, 6773–6786. <https://doi.org/10.5194/acp-11-6773-2011>

970 Guenther, A., Geron, C., Pierce, T., Lamb, B., Harley, P., Fall, R., 2000. Natural emissions of non-methane volatile organic  
971 compounds, carbon monoxide, and oxides of nitrogen from North America. *Atmospheric Environment* 34, 2205–  
972 2230.

973 Guenther, A., Hewitt, C.N., Erickson, D., Fall, R., Geron, C., Graedel, T., Harley, P., Klinger, L., Lerdau, M., McKay, W.A.,  
974 Pierce, T., Scholes, B., Steinbrecher, R., Tallamraju, R., Taylor, J., Zimmerman, P., 1995. A global model of natural  
975 volatile organic compound emissions. *Journal of Geophysical Research* 100.

976 Gunisch, M.J., May, N.W., Wen, M., Bottenus, C.L.H., Gardner, D.J., VanReken, T.M., Bertman, S.B., Hopke, P.K., Ault,  
977 A.P., Pratt, K.A., 2018. Ubiquitous influence of wildfire emissions and secondary organic aerosol on summertime  
978 atmospheric aerosol in the forested Great Lakes region. *Atmospheric Chemistry and Physics* 18, 3701–3715.  
979 <https://doi.org/10.5194/acp-18-3701-2018>

980 Holzinger, R., Lee, A., Paw, K.T., Goldstein, A.H., 2005. Observations of oxidation products above a forest imply  
981 biogenic emissions of very reactive compounds. *Atmospheric Chemistry and Physics* 5, 67–75.

982 Hu, W.W., Campuzano-Jost, P., Palm, B.B., Day, D.A., Ortega, A.M., Hayes, P.L., Krechmer, J.E., Chen, Q., Kuwata, M.,  
983 Liu, Y.J., de Sá, S.S., McKinney, K., Martin, S.T., Hu, M., Budisulistiorini, S.H., Riva, M., Surratt, J.D., St. Clair,  
984 J.M., Isaacman-Van Wertz, G., Yee, L.D., Goldstein, A.H., Carbone, S., Brito, J., Artaxo, P., de Gouw, J.A., Koss,  
985 A., Wisthaler, A., Mikoviny, T., Karl, T., Kaser, L., Jud, W., Hansel, A., Docherty, K.S., Alexander, M.L.,  
986 Robinson, N.H., Coe, H., Allan, J.D., Canagaratna, M.R., Paulot, F., Jimenez, J.L., 2015. Characterization of a real-  
987 time tracer for isoprene epoxydiols-derived secondary organic aerosol (IEPOX-SOA) from aerosol mass  
988 spectrometer measurements. *Atmospheric Chemistry and Physics* 15, 11807–11833. <https://doi.org/10.5194/acp-15-11807-2015>

989 990 991 992 IPCC (Ed.), 2007. Climate change 2007: the physical science basis: contribution of Working Group I to the Fourth  
993 Assessment Report of the Intergovernmental Panel on Climate Change. Cambridge University Press, Cambridge ;  
994 New York.

995 Jimenez, J.L., Canagaratna, M.R., Donahue, N.M., Prevot, A.S.H., Zhang, Q., Kroll, J.H., DeCarlo, P.F., Allan, J.D., Coe,  
 996 H., Ng, N.L., Aiken, A.C., Docherty, K.S., Ulbrich, I.M., Grieshop, A.P., Robinson, A.L., Duplissy, J., Smith, J.D.,  
 997 Wilson, K.R., Lanz, V.A., Hueglin, C., Sun, Y.L., Tian, J., Laaksonen, A., Raatikainen, T., Rautiainen, J.,  
 998 Vaattovaara, P., Ehn, M., Kulmala, M., Tomlinson, J.M., Collins, D.R., Cubison, M.J., Dunlea, E., Huffman, J.A.,  
 999 Onasch, T.B., Alfarra, M.R., Williams, P.I., Bower, K., Kondo, Y., Schneider, J., Drewnick, F., Borrmann, S.,  
 1000 Weimer, S., Demerjian, K., Salcedo, D., Cottrell, L., Griffin, R., Takami, A., Miyoshi, T., Hatakeyama, S.,  
 1001 Shimono, A., Sun, J.Y., Zhang, Y.M., Dzepina, K., Kimmel, J.R., Sueper, D., Jayne, J.T., Herndon, S.C., Trimborn,  
 1002 A.M., Williams, L.R., Wood, E.C., Middlebrook, A.M., Kolb, C.E., Baltensperger, U., Worsnop, D.R., 2009.  
 1003 Evolution of Organic Aerosols in the Atmosphere. *Science* 326, 1525–1529.  
 1004 <https://doi.org/10.1126/science.1180353>

1005 Jokinen, T., Berndt, T., Makkonen, R., Kerminen, V.-M., Junninen, H., Paasonen, P., Stratmann, F., Herrmann, H.,  
 1006 Guenther, A.B., Worsnop, D.R., Kulmala, M., Ehn, M., Sipilä, M., 2015. Production of extremely low volatile  
 1007 organic compounds from biogenic emissions: Measured yields and atmospheric implications. *Proceedings of the*  
 1008 *National Academy of Sciences* 112, 7123–7128. <https://doi.org/10.1073/pnas.1423977112>

1009 Kanakidou, M., Seinfeld, J.H., Pandis, S.N., Barnes, I., Dentener, F.J., Facchini, M.C., Dingenen, R.V., Ervens, B., Nenes,  
 1010 A., Nielsen, C.J., others, 2005. Organic aerosol and global climate modelling: a review. *Atmospheric Chemistry and*  
 1011 *Physics* 5, 1053–1123.

1012 Kroll, J.H., Donahue, N.M., Jimenez, J.L., Kessler, S.H., Canagaratna, M.R., Wilson, K.R., Altieri, K.E., Mazzoleni, L.R.,  
 1013 Wozniak, A.S., Bluhm, H., Mysak, E.R., Smith, J.D., Kolb, C.E., Worsnop, D.R., 2011. Carbon oxidation state as a  
 1014 metric for describing the chemistry of atmospheric organic aerosol. *Nature Chemistry* 3, 133–139.  
 1015 <https://doi.org/10.1038/nchem.948>

1016 Kruijt, B., Malhi, Y., Lloyd, J., Norbre, A.D., Miranda, A.C., Pereira, M.G.P., Culf, A., Grace, J., 2000. Turbulence  
 1017 Statistics Above And Within Two Amazon Rain Forest Canopies. *Boundary-Layer Meteorology* 94, 297–331.  
 1018 <https://doi.org/10.1023/A:1002401829007>

1019 Leong, Y.J., Sanchez, N.P., Wallace, H.W., Cevik, B.K., Hernandez, C.S., Han, Y., Flynn, J.H., Massoli, P., Floerchinger,  
 1020 C., Fortner, E.C., Herndon, S., Bean, J.K., Ruiz, L.H., Jeon, W., Choi, Y., Lefer, B., Griffin, R.J., 2017. Overview  
 1021 of surface measurements and spatial characterization of submicrometer particulate matter during the DISCOVER-  
 1022 AQ 2013 campaign in Houston, TX. *Journal of the Air & Waste Management Association* 67, 854–872.  
 1023 <https://doi.org/10.1080/10962247.2017.1296502>

1024 Makar, P.A., Staebler, R.M., Akingunola, A., Zhang, J., McLinden, C., Kharol, S.K., Pabla, B., Cheung, P., Zheng, Q., 2017.  
 1025 The effects of forest canopy shading and turbulence on boundary layer ozone. *Nature Communications* 8, 15243,  
 1026 <https://doi.org/10.1038/ncomms15243>

1027 Marais, E.A., Jacob, D.J., Jimenez, J.L., Campuzano-Jost, P., Day, D.A., Hu, W., Krechmer, J., Zhu, L., Kim, P.S., Miller,  
 1028 C.C., Fisher, J.A., Travis, K., Yu, K., Hanisco, T.F., Wolfe, G.M., Arkison, H.L., Pye, H.O.T., Froyd, K.D., Liao,  
 1029 J., McNeill, V.F., 2016. Aqueous-phase mechanism for secondary organic aerosol formation from isoprene: application to the southeast United States and co-benefit of  $\text{SO}_2$  emission controls. *Atmospheric Chemistry and*  
 1030 *Physics* 16, 1603–1618. <https://doi.org/10.5194/acp-16-1603-2016>

1031 Middlebrook, A.M., Bahreini, R., Jimenez, J.L., Canagaratna, M.R., 2012. Evaluation of Composition-Dependent Collection  
 1032 Efficiencies for the Aerodyne Aerosol Mass Spectrometer using Field Data. *Aerosol Science and Technology* 46,  
 1033 258–271. <https://doi.org/10.1080/02786826.2011.620041>

1034 Millet, D.B., Alwe, H.D., Chen, X., Deventer, M.J., Griffis, T.J., Holzinger, R., Bertman, S.B., Rickly, P.S., Stevens, P.S.,  
 1035 Léonardis, T., Locoge, N., Dusander, S., Tyndall, G.S., Alvarez, S.L., Erickson, M.H., Flynn, J.H., 2018. Bidirectional  
 1036 Ecosystem–Atmosphere Fluxes of Volatile Organic Compounds Across the Mass Spectrum: How  
 1037 Many Matter? *ACS Earth and Space Chemistry* 2, 764–777. <https://doi.org/10.1021/acsearthspacechem.8b00061>

1038 Miyazaki, Y., Fu, P., Ono, K., Tachibana, E., Kawamura, K., 2014. Seasonal cycles of water-soluble organic nitrogen  
 1039 aerosols in a deciduous broadleaf forest in northern Japan. *J. Geophys. Res. Atmos.* 119, 1440–1454.  
 1040 <https://doi.org/10.1002/2013JD020713>

1041 Mohr, C., DeCarlo, P.F., Heringa, M.F., Chirico, R., Slowik, J.G., Richter, R., Reche, C., Alastuey, A., Querol, X., Seco, R.,  
 1042 Peñuelas, J., Jiménez, J.L., Crippa, M., Zimmermann, R., Baltensperger, U., Prévôt, A.S.H., 2012. Identification  
 1043

1044 and quantification of organic aerosol from cooking and other sources in Barcelona using aerosol mass spectrometer  
 1045 data. *Atmospheric Chemistry and Physics* 12, 1649–1665. <https://doi.org/10.5194/acp-12-1649-2012>

1046 NADP, 2016. National Atmospheric Deposition Program, National Trends Network (NTN) Site Details [WWW Document].  
 1047 URL <http://nadp.slh.wisc.edu/data/sites/siteDetails.aspx?net=NTN&id=MI09> (accessed 6.21.18).

1048 Ng, N.L., Canagaratna, M.R., Zhang, Q., Jimenez, J.L., Tian, J., Ulbrich, I.M., Kroll, J.H., Docherty, K.S., Chhabra, P.S.,  
 1049 Bahreini, R., Murphy, S.M., Seinfeld, J.H., Hildebrandt, L., Donahue, N.M., DeCarlo, P.F., Lanz, V.A., Prévôt,  
 1050 A.S.H., Dinar, E., Rudich, Y., Worsnop, D.R., 2010. Organic aerosol components observed in Northern  
 1051 Hemispheric datasets from Aerosol Mass Spectrometry. *Atmospheric Chemistry and Physics* 10, 4625–4641.  
 1052 <https://doi.org/10.5194/acp-10-4625-2010>

1053 Öztürk, F., Bahreini, R., Wagner, N.L., Dubé, W.P., Young, C.J., Brown, S.S., Brock, C.A., Ulbrich, I.M., Jimenez, J.L.,  
 1054 Cooper, O.R., Middlebrook, A.M., 2013. Vertically resolved chemical characteristics and sources of submicron  
 1055 aerosols measured on a Tall Tower in a suburban area near Denver, Colorado in winter. *J. Geophys. Res. Atmos.*  
 1056 118, 2013JD019923. <https://doi.org/10.1029/2013JD019923>

1057 Paatero, P., 1997. Least squares formulation of robust non-negative factor analysis. *Chemometrics and Intelligent Laboratory*  
 1058 Systems 37, 23–35.

1059 Paatero, P., Tapper, U., 1994. Positive matrix factorization: A non-negative factor model with optimal utilization of error  
 1060 estimates of data values. *Environmetrics* 5, 111–126.

1061 Polissar, A., 1999. The aerosol at Barrow, Alaska: long-term trends and source locations. *Atmospheric Environment* 33,  
 1062 2441–2458. [https://doi.org/10.1016/S1352-2310\(98\)00423-3](https://doi.org/10.1016/S1352-2310(98)00423-3)

1063 Polissar, A.V., Hopke, P.K., Harris, J.M., 2001. Source Regions for Atmospheric Aerosol Measured at Barrow, Alaska.  
 1064 *Environ. Sci. Technol.* 35, 4214–4226. <https://doi.org/10.1021/es0107529>

1065 Pryor, S.C., Larsen, S.E., Sørensen, L.L., Barthelmie, R.J., Grönholm, T., Kulmala, M., Launiainen, S., Rannik, Ü., Vesala,  
 1066 T., 2007. Particle fluxes over forests: Analyses of flux methods and functional dependencies. *Journal of*  
 1067 *Geophysical Research* 112. <https://doi.org/10.1029/2006JD008066>

1068 Pugh, T. a. M., MacKenzie, A.R., Hewitt, C.N., Langford, B., Edwards, P.M., Furneaux, K.L., Heard, D.E., Hopkins, J.R.,  
 1069 Jones, C.E., Karunaharan, A., Lee, J., Mills, G., Misztal, P., Moller, S., Monks, P.S., Whalley, L.K., 2010.  
 1070 Simulating atmospheric composition over a South-East Asian tropical rainforest: performance of a chemistry box  
 1071 model. *Atmospheric Chemistry and Physics* 10, 279–298. <https://doi.org/10.5194/acp-10-279-2010>

1072 Rannik, Ü., Zhou, L., Zhou, P., Gierens, R., Mammarella, I., Sogachev, A., Boy, M., 2016. Aerosol dynamics within and  
 1073 above forest in relation to turbulent transport and dry deposition. *Atmospheric Chemistry and Physics* 16, 3145–  
 1074 3160. <https://doi.org/10.5194/acp-16-3145-2016>

1075 Rizzo, L.V., Artaxo, P., Karl, T., Guenther, A.B., Greenberg, J., 2010. Aerosol properties, in-canopy gradients, turbulent  
 1076 fluxes and VOC concentrations at a pristine forest site in Amazonia. *Atmospheric Environment* 44, 503–511.  
 1077 <https://doi.org/10.1016/j.atmosenv.2009.11.002>

1078 Schulze, B.C., Wallace, H.W., Bui, A.T., Flynn, J.H., Erickson, M.H., Alvarez, S., Dai, Q., Usenko, S., Sheesley, R.J.,  
 1079 Griffin, R.J., 2018. The impacts of regional shipping emissions on the chemical characteristics of coastal submicron  
 1080 aerosols near Houston, TX. *Atmospheric Chemistry and Physics* 18, 14217–14241. <https://doi.org/10.5194/acp-18-14217-2018>

1081 Schulze, B.C., Wallace, H.W., Flynn, J.H., Lefer, B.L., Erickson, M.H., Jobson, B.T., Dusanter, S., Griffith, S.M., Hansen,  
 1082 R.F., Stevens, P.S., VanReken, T., Griffin, R.J., 2017. Differences in BVOC oxidation and SOA formation above  
 1083 and below the forest canopy. *Atmospheric Chemistry and Physics* 17, 1805–1828. <https://doi.org/10.5194/acp-17-1805-2017>

1084 Seinfeld, J.H., Pandis, S.N., 2006. *Atmospheric chemistry and physics : from air pollution to climate change*. Hoboken, N.J. :  
 1085 John Wiley, ©2006.

1086 Sheesley, R.J., Schauer, J.J., Bean, E., Kenski, D., 2004. Trends in Secondary Organic Aerosol at a Remote Site in  
 1087 Michigan's Upper Peninsula. *Environmental Science & Technology* 38, 6491–6500.  
 1088 <https://doi.org/10.1021/es049104q>

1089 Sirois, A., Bottenheim, J.W., 1995. Use of backward trajectories to interpret the 5-year record of PAN and O<sub>3</sub> ambient air  
 1090 concentrations at Kejimkujik National Park, Nova Scotia. *Journal of Geophysical Research* 100, 2867.  
 1091 <https://doi.org/10.1029/94JD02951>

1094 Stein, A.F., Draxler, R.R., Rolph, G.D., Stunder, B.J.B., Cohen, M.D., Ngan, F., 2015. NOAA's HYSPLIT Atmospheric  
1095 Transport and Dispersion Modeling System. *Bulletin of the American Meteorological Society* 96, 2059–2077.  
1096 <https://doi.org/10.1175/BAMS-D-14-00110.1>

1097 Steiner, A.L., Pressley, S.N., Botros, A., Jones, E., Chung, S.H., Edburg, S.L., 2011. Analysis of coherent structures and  
1098 atmosphere-canopy coupling strength during the CABINEX field campaign. *Atmospheric Chemistry and Physics*  
1099 11, 11921–11936. <https://doi.org/10.5194/acp-11-11921-2011>

1100 Stroud, C., Makar, P., Karl, T., Guenther, A., Geron, C., Turnipseed, A., Nemitz, E., Baker, B., Potosnak, M., Fuentes, J.D.,  
1101 2005. Role of canopy-scale photochemistry in modifying biogenic-atmosphere exchange of reactive terpene  
1102 species: Results from the CELTIC field study. *Journal of Geophysical Research: Atmospheres* 110.  
1103 <https://doi.org/10.1029/2005JD005775>

1104 Thomas, C., Foken, T., 2007. Flux contribution of coherent structures and its implications for the exchange of energy and  
1105 matter in a tall spruce canopy. *Boundary-Layer Meteorology* 123, 317–337. <https://doi.org/10.1007/s10546-006-9144-7>

1106 Thornberry, T., Carroll, M.A., Keeler, G.A., Sanford, S., Bertman, S.B., Pippin, M.R., Ostling, K., Grossenbacher, J.W.,  
1107 Shepson, P.B., Cooper, O.R., Moody, J.L., Stockwell, W.R., 2001. Observations of reactive oxidized nitrogen and  
1108 speciation of NO<sub>x</sub> during the PROPHET summer 1998 intensive. *Journal of Geophysical Research* 106, 359–386.

1109 Toma, S., Bertman, S., 2012. The atmospheric potential of biogenic volatile organic compounds from needles of white pine  
1110 (*Pinus strobus*) in Northern Michigan. *Atmospheric Chemistry and Physics* 12, 2245–2252.  
1111 <https://doi.org/10.5194/acp-12-2245-2012>

1112 Ulbrich, I.M., Canagaratna, M.R., Zhang, Q., Worsnop, D.R., Jimenez, J.L., 2009. Interpretation of organic components  
1113 from Positive Matrix Factorization of aerosol mass spectrometric data. *Atmospheric Chemistry and Physics* 9,  
1114 2891–2918.

1115 US Census Bureau, 2018. City and Town Population Totals: 2010–2016 [WWW Document]. URL  
1116 <https://www.census.gov/data/tables/2016/demo/popest/total-cities-and-towns.html> (accessed 1.24.18).

1117 VanReken, T.M., Mwaniki, G.R., Wallace, H.W., Pressley, S.N., Erickson, M.H., Jobson, B.T., Lamb, B.K., 2015. Influence  
1118 of air mass origin on aerosol properties at a remote Michigan forest site. *Atmospheric Environment* 107, 35–43.  
1119 <https://doi.org/10.1016/j.atmosenv.2015.02.027>

1120 Wallace, H.W., Sanchez, N.P., Flynn, J.H., Erickson, M.H., Lefer, B.L., Griffin, R.J., 2018. Source apportionment of  
1121 particulate matter and trace gases near a major refinery near the Houston Ship Channel. *Atmospheric Environment*  
1122 173, 16–29. <https://doi.org/10.1016/j.atmosenv.2017.10.049>

1123 Wang, Y.Q., 2014. MeteoInfo: GIS software for meteorological data visualization and analysis: Meteorological GIS  
1124 software. *Meteorological Applications* 21, 360–368. <https://doi.org/10.1002/met.1345>

1125 Wang, Y.Q., Zhang, X.Y., Draxler, R.R., 2009. TrajStat: GIS-based software that uses various trajectory statistical analysis  
1126 methods to identify potential sources from long-term air pollution measurement data. *Environmental Modelling &*  
1127 *Software* 24, 938–939. <https://doi.org/10.1016/j.envsoft.2009.01.004>

1128 Whitehead, J.D., Gallagher, M.W., Dorsey, J.R., Robinson, N., Gabey, A.M., Coe, H., McFiggans, G., Flynn, M.J., Ryder,  
1129 J., Nemitz, E., Davies, F., 2010. Aerosol fluxes and dynamics within and above a tropical rainforest in South-East  
1130 Asia. *Atmospheric Chemistry and Physics* 10, 9369–9382. <https://doi.org/10.5194/acp-10-9369-2010>

1131 Wiedinmyer, C., Greenberg, J., Guenther, A., Hopkins, B., Baker, K., Geron, C., Palmer, P.I., Long, B.P., Turner, J.R.,  
1132 Pétron, G., Harley, P., Pierce, T.E., Lamb, B., Westberg, H., Baugh, W., Koerber, M., Janssen, M., 2005. Ozarks  
1133 Isoprene Experiment (OZIE): Measurements and modeling of the “isoprene volcano.” *Journal of Geophysical  
1134 Research: Atmospheres* 110. <https://doi.org/10.1029/2005JD005800>

1135 Wolfe, G.M., Thornton, J.A., 2011. The Chemistry of Atmosphere-Forest Exchange (CAFE) Model – Part 1: Model  
1136 description and characterization. *Atmospheric Chemistry and Physics* 11, 77–101. <https://doi.org/10.5194/acp-11-77-2011>

1137 Xu, L., Pye, H.O.T., He, J., Chen, Y.L., Murphy, B.N., Ng, N.L., 2018. Experimental and model estimates of the  
1138 contributions from biogenic monoterpenes and sesquiterpenes to secondary organic aerosol in the southeastern  
1139 United States. *Atmospheric Chemistry and Physics* 18, 12613–12637. <https://doi.org/10.5194/acp-18-12613-2018>

1140 Xu, L., Suresh, S., Guo, H., Weber, R.J., Ng, N.L., 2015. Aerosol characterization over the southeastern United States using  
1141 high-resolution aerosol mass spectrometry: spatial and seasonal variation of aerosol composition and sources with a  
1142

1144 focus on organic nitrates. *Atmospheric Chemistry and Physics* 15, 7307–7336. <https://doi.org/10.5194/acp-15-7307-2015>

1145 Zhang, Q., Jimenez, J.L., Canagaratna, M.R., Allan, J.D., Coe, H., Ulbrich, I., Alfarra, M.R., Takami, A., Middlebrook, A.M., Sun, Y.L., Dzepina, K., Dunlea, E., Docherty, K., DeCarlo, P.F., Salcedo, D., Onasch, T., Jayne, J.T., Miyoshi, T., Shimono, A., Hatakeyama, S., Takegawa, N., Kondo, Y., Schneider, J., Drewnick, F., Borrmann, S., Weimer, S., Demerjian, K., Williams, P., Bower, K., Bahreini, R., Cottrell, L., Griffin, R.J., Rautiainen, J., Sun, J.Y., Zhang, Y.M., Worsnop, D.R., 2007. Ubiquity and dominance of oxygenated species in organic aerosols in anthropogenically-influenced Northern Hemisphere midlatitudes: Ubiquity and dominance of oxygenated OA. *Geophysical Research Letters* 34, 6. <https://doi.org/10.1029/2007GL029979>

1146 Zhang, Q., Jimenez, J.L., Canagaratna, M.R., Ulbrich, I.M., Ng, N.L., Worsnop, D.R., Sun, Y., 2011. Understanding atmospheric organic aerosols via factor analysis of aerosol mass spectrometry: a review. *Analytical and Bioanalytical Chemistry* 401, 3045–3067. <https://doi.org/10.1007/s00216-011-5355-y>

1147 Zhang, Q., Worsnop, D.R., Canagaratna, M.R., Jimenez, J.L., 2005. Hydrocarbon-like and oxygenated organic aerosols in Pittsburgh: insights into sources and processes of organic aerosols. *Atmospheric Chemistry and Physics* 5, 3289–3311.

1148

1149

1150

1151

1152

1153

1154

1155

1156

1157

1158

**Page 6: [1] Deleted**

**Microsoft Office User**

**10/13/21 8:12:00 PM**

**X**

.....